NUREG/CR-0120
ORNL/NUREG/TM-163

Effect of Energy Density on Aerosol Yield and Primary Particle Sizes Produced by the Capacitor Discharge Vaporization (CDV) of UO_2

A. L. Wright
H. W. Bertini
T. S. Kress
M. L. Tobias
M. J. Kelly
L. F. Parsly
J. S. White

Prepared for the U.S. Nuclear Regulatory Commission
Office of Nuclear Regulatory Research
Under Interagency Agreements DOE 40-551-75 and 40-552-75

OAK RIDGE NATIONAL LABORATORY
OPERATED BY UNION CARBIDE CORPORATION · FOR THE DEPARTMENT OF ENERGY

Printed in the United States of America. Available from
National Technical Information Service
U.S. Department of Commerce
5285 Port Royal Road, Springfield, Virginia 22161

NUREG/CR-0120
ORNL/NUREG/TM-163
Dist. Category R7

Contract No. W-7405-eng-26

Engineering Technology Division

EFFECT OF ENERGY DENSITY ON AEROSOL YIELD AND PRIMARY PARTICLE SIZES PRODUCED BY THE CAPACITOR DISCHARGE VAPORIZATION (CDV) OF UO_2

A. L. Wright
H. W. Bertini M. J. Kelly
T. S. Kress L. F. Parsly
M. L. Tobias J. S. White

Manuscript Completed — August 31, 1978

Date Published — October 1978

Prepared for the
U.S. Nuclear Regulatory Commission
Office of Nuclear Regulatory Research
Under Interagency Agreements DOE 40-551-75 and 40-552-75

NRC FIN No. B0121

Prepared by the
OAK RIDGE NATIONAL LABORATORY
Oak Ridge, Tennessee 37830
operated by
UNION CARBIDE CORPORATION
for the
DEPARTMENT OF ENERGY

CONTENTS

SUMMARY

The Aerosol Release and Transport (ART) Program at ORNL is developing a technique for using electrical energy stored in capacitors to place small samples of LMFBR fuel into very high energy states representative of those calculated for severe hypothetical core-disruptive accidents (HCDAs). The ART program is sponsored by the Advanced Reactor Safety Research Division of the Nuclear Regulatory Commission. The capacitor discharge vaporization (CDV) tool is used in the program in a variety of experiments related to the HCDA source term and to the resultant fuel aerosol properties and behavior.

This technique is being developed in the CRI-III/CDV portion of the ART program in which the high-energy molten fuel (UO_2) is allowed to undergo free expansion into the CRI-III vessel filled with room-temperature argon at 1 atm pressure. As part of this development effort, tests have been conducted in which the major objectives have been to establish the airborne mass (yield) and the size distribution of the primary aerosols as functions of the maximum energy content of the fuel before free expansion. The results of these so-called "upper-limit" tests are discussed in this report.

In general, at high energy ($\sim$3000 J/g) the yields (measured airborne mass) have been considerably less (about a factor of 1/5) than would be expected from equilibrium thermodynamic expansion calculations. At lower energies (<2000 J/g) the yields exceeded the predicted values. Attempts are made to explain the difference at high energies in terms of potential energy losses and errors in the experimental measurements. Some potential effects were identified, but a definitive explanation for the differences was not established. Additional tests were identified that may be useful in resolving the unanswered questions in future experiments, and the analytical efforts to explain the differences will continue.

The size distributions of the primary aerosol particles formed by nucleation and growth from the vapor state were measured directly from electron photomicrographs of samples collected on precipitator grids. The primary sizes were small, ranging from >0.004 to 0.1 μ in diameter. The distribution of sizes was essentially independent of the initial

energy state of the molten fuel over the range covered. The size distribution is log-normal with a mean geometric diameter d_g of 0.014 μ and a standard deviation σ_g of 1.8.

The measured size data may be useful in determining the properties of the agglomerates for direct input into aerosol behavioral codes when applied to the HCDA bubble or for cases of direct fuel vapor release into the secondary containment.

GLOSSARY OF ACRONYMS

AEDC	Arnold Engineering Development Center
ART	Aerosol Release and Transport
CDV	Capacitor Discharge Vaporization
CRI*	Containment Research Installation
FAST	Fuel Aerosol Simulant Test
HCDA	Hypothetical Core-Disruptive Accident
LMFBR	Liquid-Metal Fast Breeder Reactor
NRC	Nuclear Regulatory Commission
ORNL	Oak Ridge National Laboratory

---

*Historic designation of a location rather than the name of the current activity.

EFFECT OF ENERGY DENSITY ON AEROSOL YIELD AND PRIMARY PARTICLE SIZES PRODUCED BY THE CAPACITOR DISCHARGE VAPORIZATION (CDV) OF UO_2

A. L. Wright
H. W. Bertini M. J. Kelly
T. S. Kress L. F. Parsly
M. L. Tobias J. S. White

ABSTRACT

This report documents experimental results obtained in the CRI-III/CDV portion of the ORNL Aerosol Release and Transport (ART) Program, sponsored by the Advanced Reactor Safety Research Division of the Nuclear Regulatory Commission. In the CRI-III/CDV program, the capacitor discharge vaporization (CDV) technique is used to bring simulant LMFBR fuel samples (UO_2) to energy states representative of those calculated for severe hypothetical core-disruptive accidents (HCDAs). The high-energy molten UO_2 undergoes a free expansion in the CRI-III vessel, and the vapor produced converts to an aerosol. This report discusses the results of tests where the major objective was to establish the UO_2 aerosol mass made airborne (yield) and the size distribution of the primary aerosol as a function of the energy content of the UO_2 before expansion.

1. INTRODUCTION

The capacitor discharge vaporization (CDV) experiments were described in the work plan for the ART program.[1] Briefly, the aim of the CDV effort is to develop a technique using electrical energy stored in capacitors to place LMFBR fuel into high energy states representative of those calculated for severe hypothetical core-disruptive accidents (HCDAs). The sudden disruption of the fuel element samples (UO_2) by internal pressure generated by the capacitor discharge and the expected unattenuated character of the subsequent expansion give these experiments the name of "upper-limit source term" tests.

The CDV technique is discussed in detail in Section 2, and an extensive discussion of the development of the method is given in another report.[2] The main features of the method at its present stage of development are the following. Test specimens of UO_2 in specially designed

sample holders are preheated by the direct application of electrical energy until a substantial portion is molten, and then four banks of 2500-V capacitors are applied to the circuit. The subsequent capacitor discharge increases the energy content of the molten UO_2 and internal pressure ruptures a quartz containment. On expanding into the argon-filled CRI-III vessel, the UO_2 flashes into vapor. The discharge is monitored by a high-speed color camera; voltage, current, and sample temperature are also recorded using high-speed recording oscilloscopes. The CDV system produces energy deposition rates and total energy per gram comparable to those expected in an HCDA (10^6 J/g-s and up to 3000 J/g total).

Aerosol sampling begins about 2 min after capacitor discharge. The samples taken include transient airborne mass concentrations, transient aerosol sizes, and electron microscope grid samples of the settled agglomerates.

Section 2 of this report describes the CRI-III/CDV facility in more detail. Section 3 gives the measured yield results (ratios of airborne mass to initial mass of molten UO_2), a discussion of the modeling of the energy deposition during preheat and capacitor discharge, and methods of determining vapor yield by assuming constant internal energy and isentropic expansion of UO_2 after capacitor discharge. Large discrepancies between predicted and observed aerosol yields are noted, and possible energy losses and measurement errors which might account for the low yields are discussed. Rough estimates are made of effects such as radiation losses from an initial cloud of vaporizing drops and of cooling and condensing of hot vapor onto UO_2 microspheres.

The primary size measurement results, taken directly from the electron photomicrographs, are presented in Section 4. These show that the primary aerosol sizes are small (ranging from 0.004 to 0.1 μ in diameter) and that the size distribution is relatively insensitive to CDV energy density. A cumulative probability plot of the data shows that the distribution is log-normal with a mean geometric diameter d_g of 0.014 μ and a standard deviation σ_g of 1.8. The significance of these size measurements to HCDAs is also discussed in Section 4.

The possible conclusions are summarized and recommendations are made for experimental studies needed to resolve the issues raised by the work done thus far.

2. TEST FACILITY DESCRIPTION AND EXPERIMENTAL DATA REDUCTION

2.1 Description of the CRI-III/CDV Facility

The CRI-III/CDV facility, which consists of an aerosol test vessel, the CDV system and associated controls, and the data acquisition equipment, is shown in Figs. 2.1 and 2.2. The key to the various parts of the facility is given below.

Key to Fig. 2.1 (experimental area)

1. Capacitor energy storage bank enclosure with electronic test equipment in open door.
2. Preheater for sample conditioning prior to high energy insertion (floor rack).
3. Junction box where preheat power and capacitor discharge current are measured and switched. Heavy copper coaxial cable is connected to test sample.
4. Pyrometer and high-speed camera (on tripods) focused on sample visible through optical port.
5. Test vessel. Five access flanges on lower section are for sample insertion and optical and electrical diagnostic equipment installation. The two large flanges at the vessel midline contain rotary samplers for serial sampling of aerosol plateout and concentration. On top is an Andersen sampler used to determine aerosol dynamic properties with time.
6. Vacuum pump and argon-addition system.
7. Heater control equipment for vessel heaters.

Key to Fig. 2.2 (experimental control and data acquisition area)

1. TV monitoring equipment. Upper screen is preheat monitor and shows test sample in vessel. Lower screen shows experimental area and is a safety monitor during tests.
2. Electrical data acquisition and firing control equipment: (a) Timing and sequencing equipment for preheat program, camera start and bank

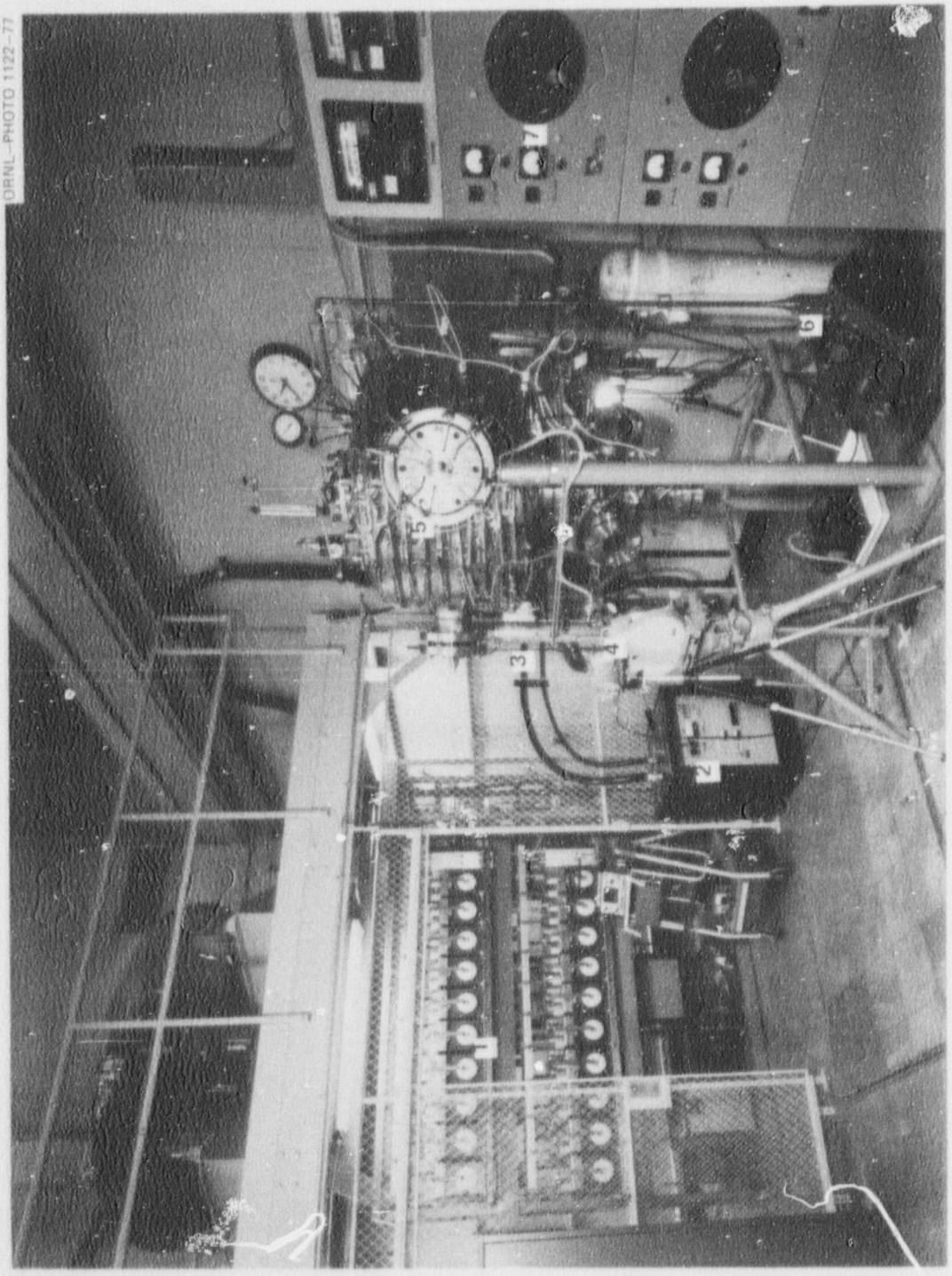

Fig. 2.1. Overall view of operational area for CRI-III/CDV experiments.

Fig. 2.2. Experimental control and data acquisition area for CRI-III/CDV tests.

firing; (*b*) four-channel tape recorder for transient data acquisition and storage; (*c*) digital two-channel storage oscilloscope used for temperature recording during sample disassembly and other selected measurements; (*d*) two-channel storage oscilloscope to record sample voltage and current during capacitor bank firing; (*e*) four-channel recorder to measure preheat cycle voltage, current, and power.

3. Master safety interlock.
4. Capacitor bank charging control panel.
5. X-Y plotter used to convert data to graphical format.
6. Video tape recorder to provide permanent preheat cycle visual record.

The test vessel is approximately 107 cm (42 in.) in diam and 89 cm (35 in.) high; it has an available internal volume of 0.56 m^3 (1.98×10^1 ft^3). The vessel is code certified to 1.06 MPa (140 psig) at 811 K (1000°F). A lower chamber, flanged to accept the CDV vaporizer unit, is equipped with quartz view windows to permit tests to be recorded by high-speed photography and to permit radiation pyrometer temperature measurements. Aerosol characterization equipment, described later, is attached to the upper vessel ports.

Two CDV vaporizer designs are shown in Figs. 2.3 and 2.4. Electrical current flows through a central conductor, a tungsten electrode, and then through the test sample. The lower electrode receives current from the sample and conducts it to the outer stainless steel tubing return path, which is coaxial with the UO_2.

Test samples consisted of a stack of UO_2 pellets surrounded by loose UO_2 microsphere [diameters from 0.035–0.050 cm (0.014–0.020 in.)] or powder packing. The pellet/microsphere assembly is housed in an outer quartz sheath, which is necessary for containment during preheat. The microsphere packing serves as thermal insulation to prevent quartz melting during sample preheat and inhibits bypass arcing around the pellet stack during capacitor discharge. The pellets are spring-loaded between tungsten electrodes to allow for expansion during preheat.

Samples for the test cases varied in length between 9 and 11.5 cm (3.54 and 4.53 in.) and had 0.5-cm (0.20-in.) diameters. The microsphere packing extended to the inner surface of the quartz tube, which had an

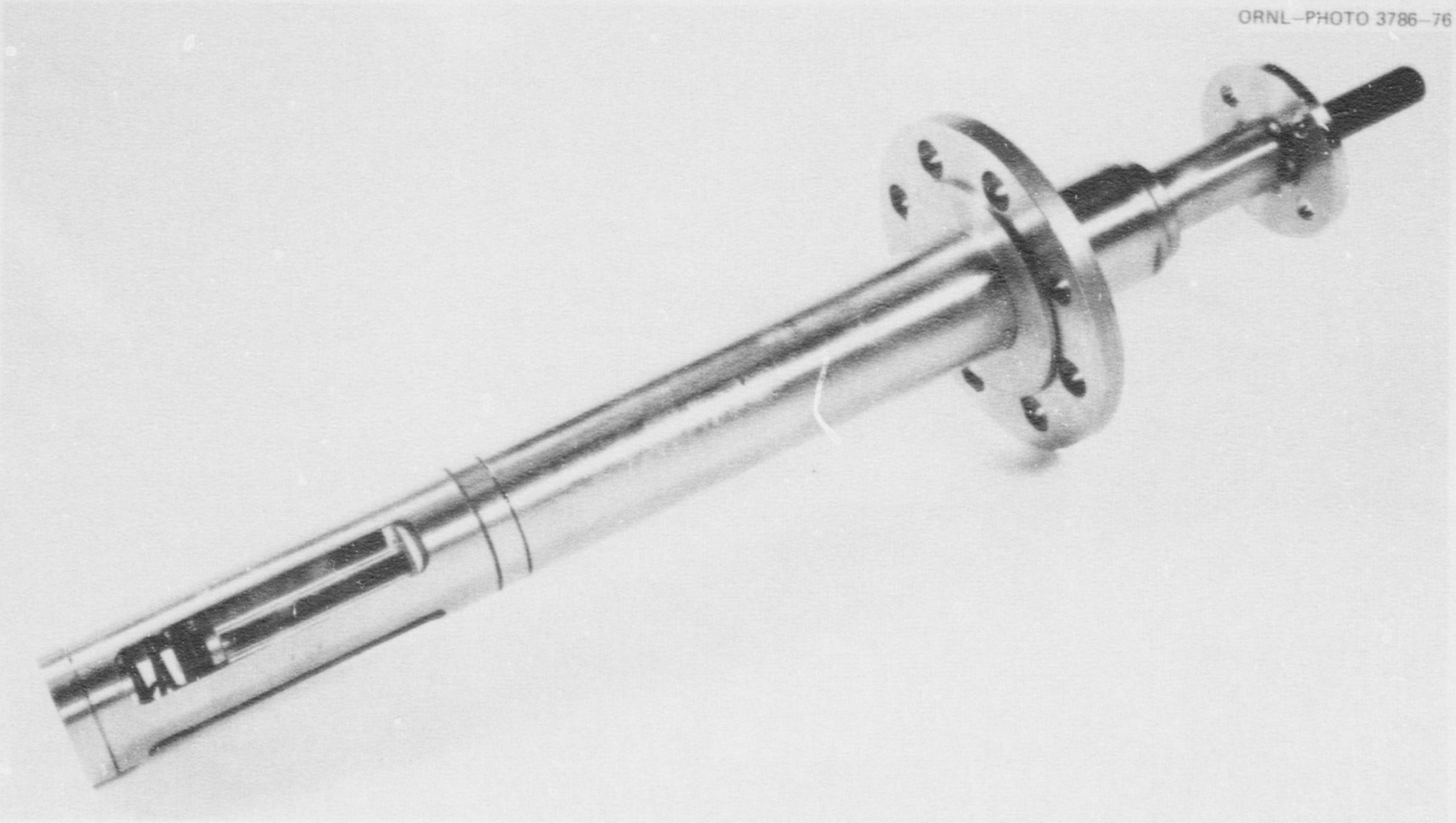

Fig. 2.3. Test sample used in CRI-III tests 1–15.

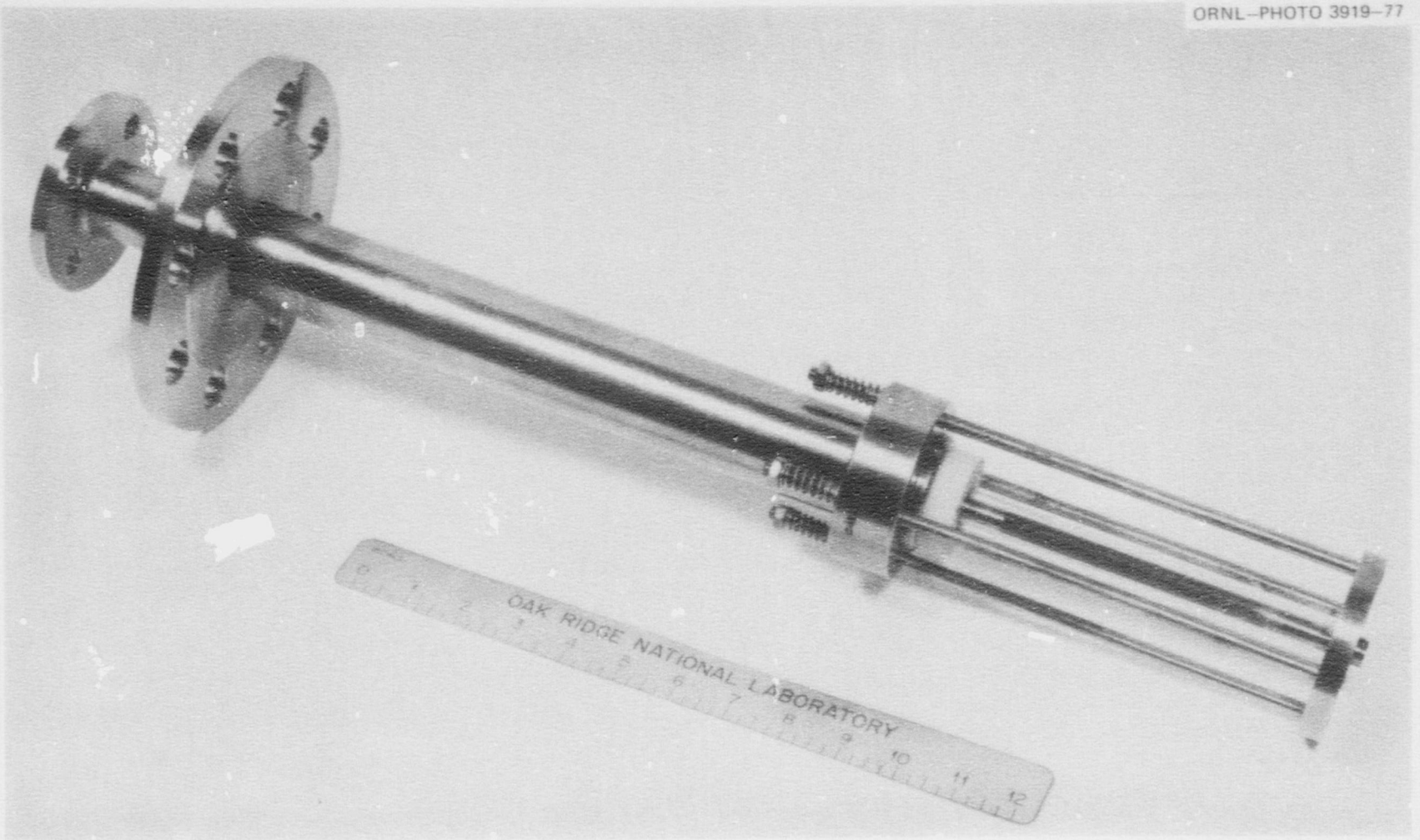

Fig. 2.4. Present standard CRI-III sample.

inner diameter of about 1 cm (2.54 in.). Nominal sample loading is 2 g of pellet and 3+ g of microspheres per centimeter of length.

The sample configuration shown in Fig. 2.3 was used in CDV tests 1–15. A new design, shown in Fig. 2.4, was used in subsequent tests in order to reduce arcing between the upper tungsten electrode and the current return path and to reduce the amount of surface area exposed to the expanding hot vapor.

In a typical experiment, pellets are preheated to an assumed fully melted condition (preheat tests indicate that full melting occurred). Uranium dioxide has a highly negative dependence of resistance with temperature proportional to T^{-5}. At room temperature, the resistance of UO_2 is approximately 10^6 Ω; therefore, preheating is needed to bring the sample to a conductivity at which it can accept high rates of power input ($\sim 10^5$ W/g).

However, stable control of this preheat is difficult due to the large change in resistivity with temperature. A constant power controller was designed[2] to deliver a full-range average load power of 4 kW from a single-phase, 120-V, 60-Hz source. Power control is achieved using conduction angle control (phase firing) of inverse-parallel silicon-controlled rectifiers (SCRs). The test sample is first heated until its resistance is ∿100 Ω; then the constant power preheater is used to melt the pellet stack. Sample resistance at the end of preheat is ≤0.5 Ω.

After the preheater is disconnected from the sample, the capacitors are discharged through the pellet stack until the internal pressure fractures the quartz containment. High-pressure UO_2 then flash-evaporates into the argon atmosphere and, after mixing with the argon, condenses into an aerosol.

The capacitor bank system consists of four modules, each containing ten capacitors rated for 3 kJ at 2500 V. The modules are connected in parallel, allowing various combinations of module discharge to be employed. Energy deposition rates between 0.4 and 1.2 MW/g have been achieved, and the UO_2 samples have been placed into average energy states calculated to be as high as 3000 J/g.

Data acquisition for the CRI-III experiments is concentrated on two phases: (1) energy input to the pellets and (2) the history and properties of the aerosol produced.

Voltage, current, and power into the sample during high preheat are recorded on a four-channel strip-chart recorder, and the sample is monitored by a television camera.

During capacitor discharge, the transient voltage and current into the sample are converted to suitable amplitudes and recorded. Signal conditioners for load voltage and current can reproduce the transient waveforms within ±2% with a response time of 30 μsec. Also during this phase, the sample is monitored using a high-speed color camera (10,000 frames/sec) and a high-speed radiation pyrometer focused on the sample.

Pyrometer measurement results for two CRI-III tests are shown in Fig. 2.5. These results indicate that high UO_2 energy states are achieved

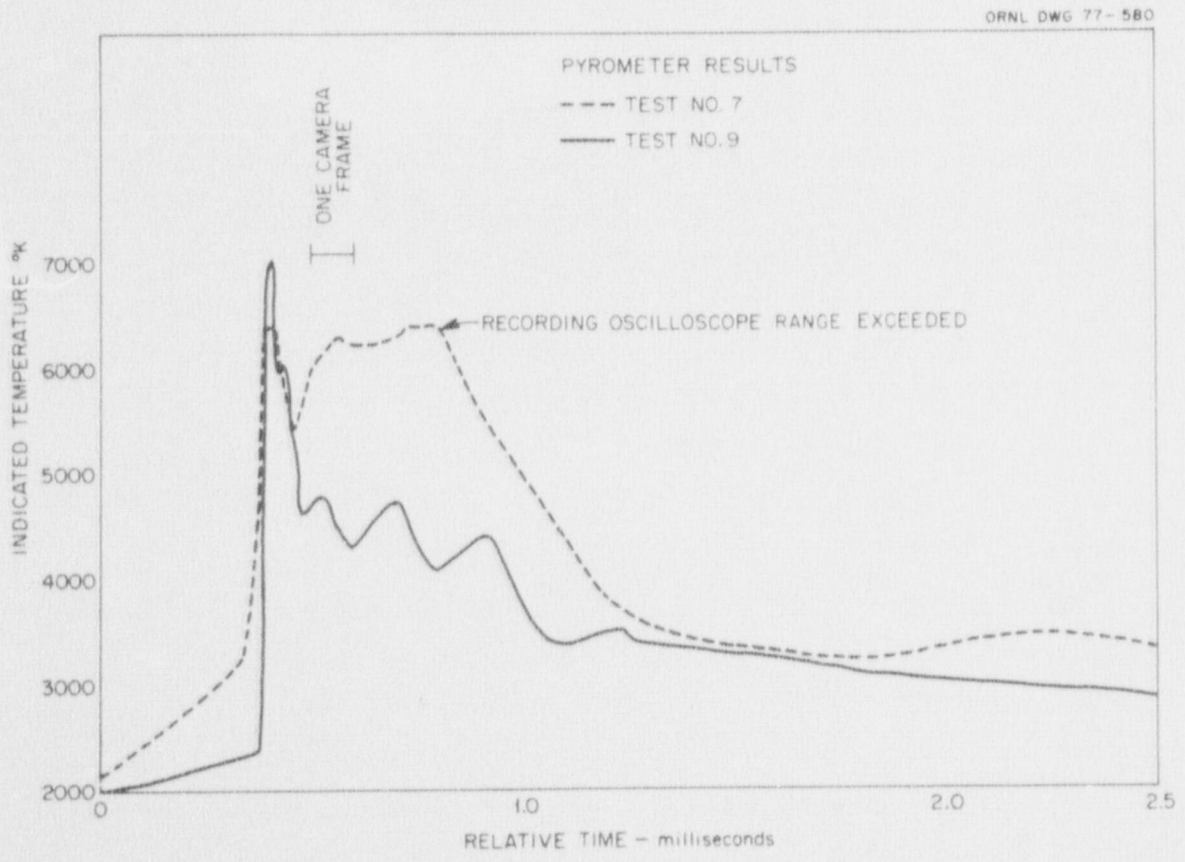

Fig. 2.5. Optical pyrometer temperature measurements for selected CRI-III tests.

corresponding to temperatures greater than 6000 K (10,340°F) in the expanding vapor cloud.

A two-channel storage oscilloscope and a two-channel digital storage oscilloscope are used to record the fast-response signals. The former produces permanent photographic records of data and the latter digitizes analog data as rapidly as 0.5 μsec/point. As a backup storage system, a four-channel 15-kH frequency response tape recorder is connected in parallel to the storage oscilloscopes.

Sampling of the particulate matter suspended in the vessel begins ∿2 min after capacitor discharge. Within the first 2 min, any large (>4-μm-diam) particles that may have been produced by fractionating of the liquid are expected to have been precipitated to the vessel floor.

Aerosol mass concentration is determined using a sequential mass sampler as shown in Fig. 2.6. The normal sample volume taken through each filter is 5 liters. The collected mass determines the suspended aerosol concentration at a given time after capacitor discharge.

Plateout samplers equipped with electron microscope grid precipitators are also used; they are shown in Fig. 2.7 with the sampler cover plate removed. Chemical analysis of collection coupons for a given exposure time allows plateout rates to be determined. The transmission electron photomicrographs of the grid samples are analyzed directly to determine the size distribution of primary particles and the nature of agglomerates. Both the plateout and sequential mass samplers are mounted flush with the vessel wall at its midline.

Other aerosol samplers used include electrostatic precipitators, Andersen cascade impactors, and condensation nuclei counters. The aerodynamic size distribution of the agglomerated aerosol is determined from cascade impactor samples. Particle number counts (number/cm^3) are determined with the condensation nuclei counter. This device has an upper limit of $\sim 10^7$ particles/cm^3; the number count generally does not fall to this level in the CRI-III vessel until about 15 min after capacitor discharge.

A more detailed description of the facility and measurement instrumentation can be found in Ref. 2.

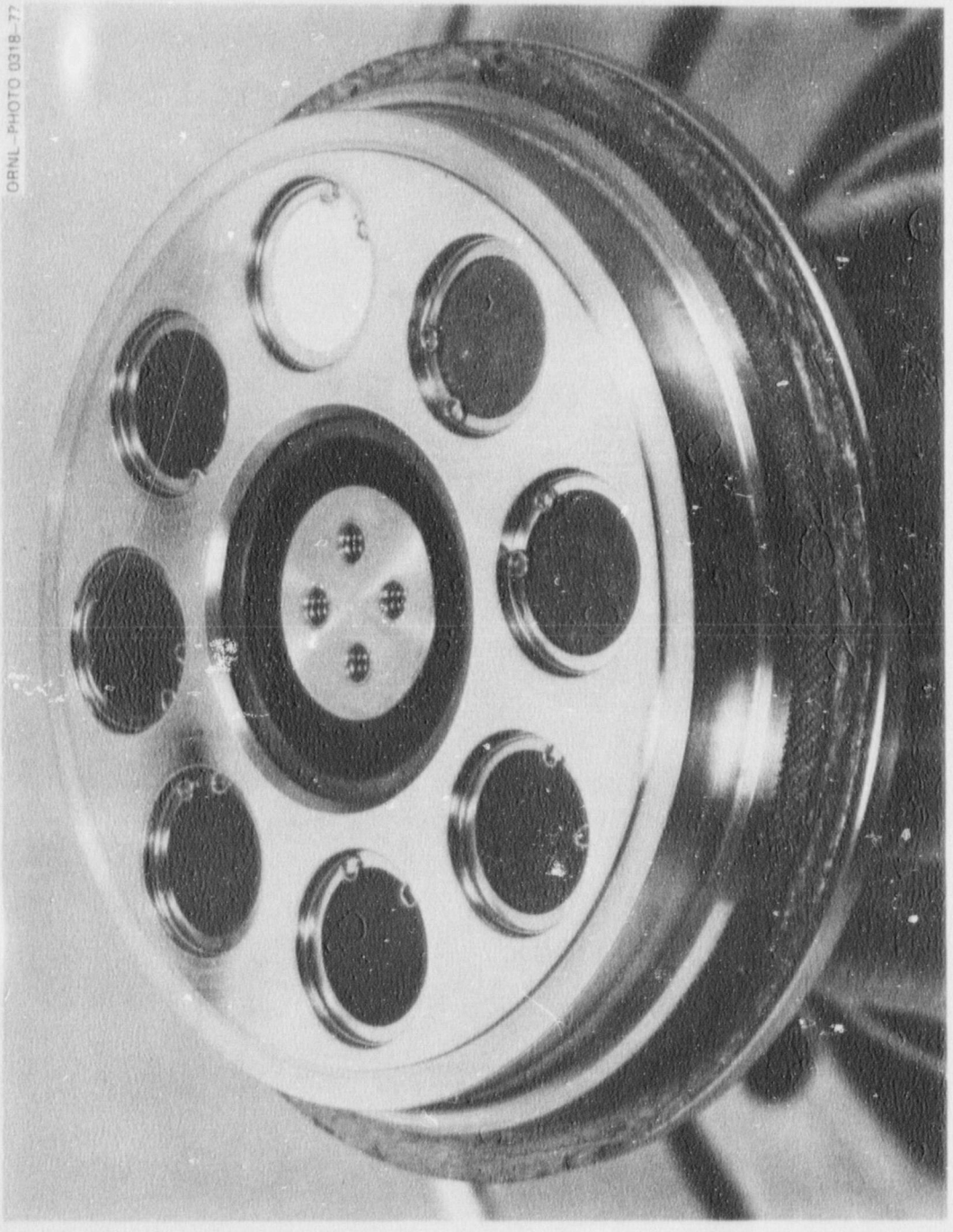

Fig. 2.6. Aerosol concentration sampler after use with front cover plate removed.

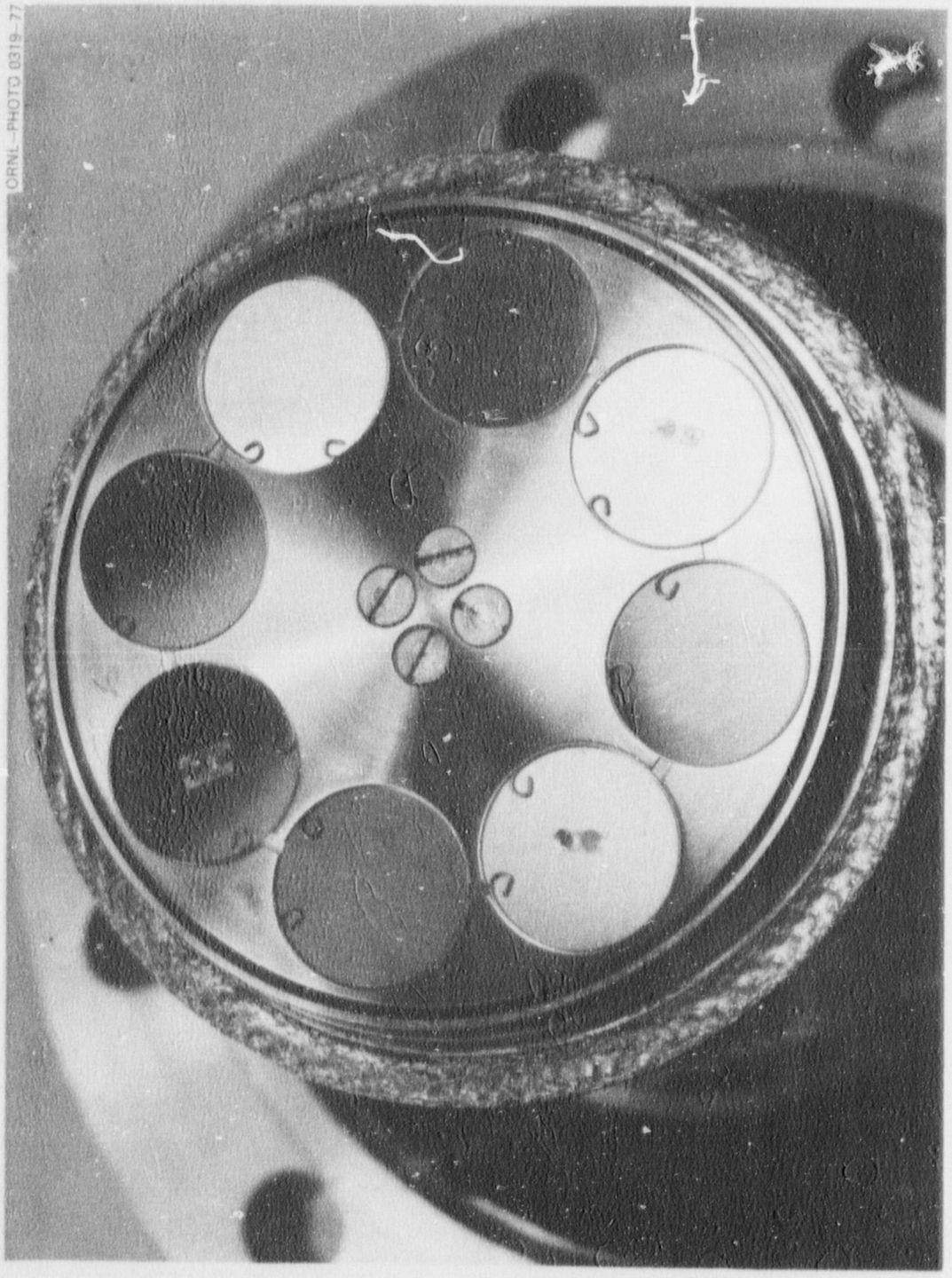

Fig. 2.7. Plateout sampler with front cover plate removed showing attached photomicrograph grids.

2.2 Data Reduction in CRI-III/CDV Tests

Table 2.1 presents a physical description of the test samples, two of which had thorium oxide (ThO_2) microsphere packing rather than UO_2 packing.

Table 2.2 presents raw data for the preheat and capacitor discharge phases and values of the initial aerosol yield. The preheat values are preset on the power controller; the amount of energy deposited during capacitor discharge is determined from the voltage and current data recorded on fast-response oscilloscopes. Input power to the sample (power = voltage × current) is integrated over time up to the time of arcing to determine total CDV energy into the pellet stack. By comparison of current vs time traces with the high-speed movies, the occurrence of arcing is found to correspond to the time when the quartz ruptures. Once an arc is produced, either to the electrical return path or to argon in the vessel, energy is no longer deposited into the sample.

Aerosol yield is determined by fitting the mass concentration vs time data with an appropriate curve. Typical plots of concentration vs tim for CRI-III tests are shown in Fig. 2.8. Initial yield is estimated by extrapolating a least-squares fit of the data to zero time, assuming a first-order exponential dependence of concentration vs time.

Table 2.3 presents the energy vs yield data determined on a consistent basis – net energy into the pellet stack, calculated from 298 K (73°F) per gram of pellet, and aerosol yield in grams per gram of pellet. Tests that included ThO_2 microspheres were used to determine the partitioning of input energy between the pellets and microspheres during preheat and capacitor discharge. Thorium oxide is a good electrical insulator compared to UO_2 and has similar thermal properties. Comparison plots of preheat power vs sample resistance for samples containing UO_2 and ThO_2 microspheres show that, at powers of 250 W/cm, approximately 25% of the input power went into the UO_2 microspheres. Thus, gross power inputs were scaled to input power per gram of pellet by using a 0.75 correction factor. CDV energy input per pellet gram is found using a 0.75 scaling factor for low energy depositions and 0.8 for high energy inputs.

Table 2.1. Physical description of samples for energy density tests

CDV No.	Quartz ID-OD (mm)	Nominal length (cm)	Pellet mass (g)	Microsphere mass (g)
2	10.4-18	9	19.71	36.6
3	10.4-20	9	20.44	34.8
4	10.4-20	9	18.98	36.8
7	10.4-20	9	17.52	37.4
12	10.4-20	9	18.98	35.8
15	10.4-20	9	17.52	32.9
16	10.4-20.4	10.5	20.44	35.4
17	10.4-20.4	11.0	21.90	36.8
19	10.0-20.4	10.8	21.90	35.4
22	10.0-20	11.5	23.36	37.3
25	10.4-20	11.5	23.36	35.1
29	10.0-20.4	11.5	23.84	37.3
9	10.5-18	9	18.98	30.2[a]
21	10.4-20	11	21.90	30.6[b]
24	10.4-20	11	21.90	33.5[b]

[a] Also 1.8 g of stainless filings.

[b] ThO_2 microsphere packing.

Table 2.2. Observed data and results for energy density tests

CDV No.	High preheat power (W)	Final resistance (Ω)	Bank deposited (kJ)	Aerosol yield ($\mu g/cm^3$)
2	2080	0.40	27.9	5.34
3	2280	0.38	3.2	0.58
4	2400	0.31	12.3	1.29
7	2400	0.35	19.8	2.04
12	2360	0.27	3+	1.35
15	1960	0.24	3.2	1.21
16	2000	0.42	25.2	2.81
17	2200	0.41	29.7	2.99
19	2400	0.31	4.3	0.81
22	2200	0.39	8.0	0.97
25	2300	0.41	11.2	1.07
29	2650	0.35	5.8	0.92
9	2400	0.35	29.2	3.61
21	2200	0.51	33.9	2.50
24	2200	0.60	32.9	1.96

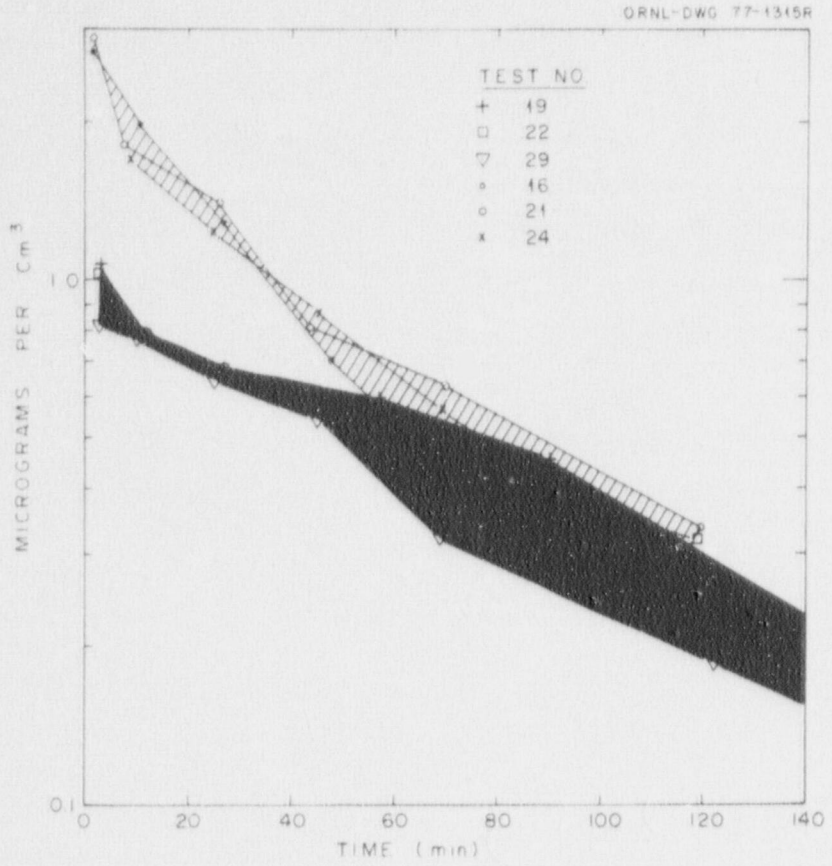

Fig. 2.8. Aerosol concentration vs time for selected CRI-III tests.

(This assumption is justified by computer calculations for energy input during capacitor discharge.)

Net energy into the sample per gram of pellet from 298 K (73°F) includes the energy from preheat plus energy added by capacitor discharge. The minimum addition during preheat is 1400 J/g to uniformly melt the pellets at 3123 K (5162°F), plus 200 J/g to account for the thermal gradient across the pellet stack. Accounting for differences in preheat power and effects of radiation heat loss, this results in a maximum of 1680 J/g.

Figure 2.9 is a plot of aerosol yield vs normalized input energy to the pellets. Since it is assumed that all vapor produced becomes an aerosol, aerosol yield can be interpreted as vapor yield. The analysis discussed in Section 3 explains this data.

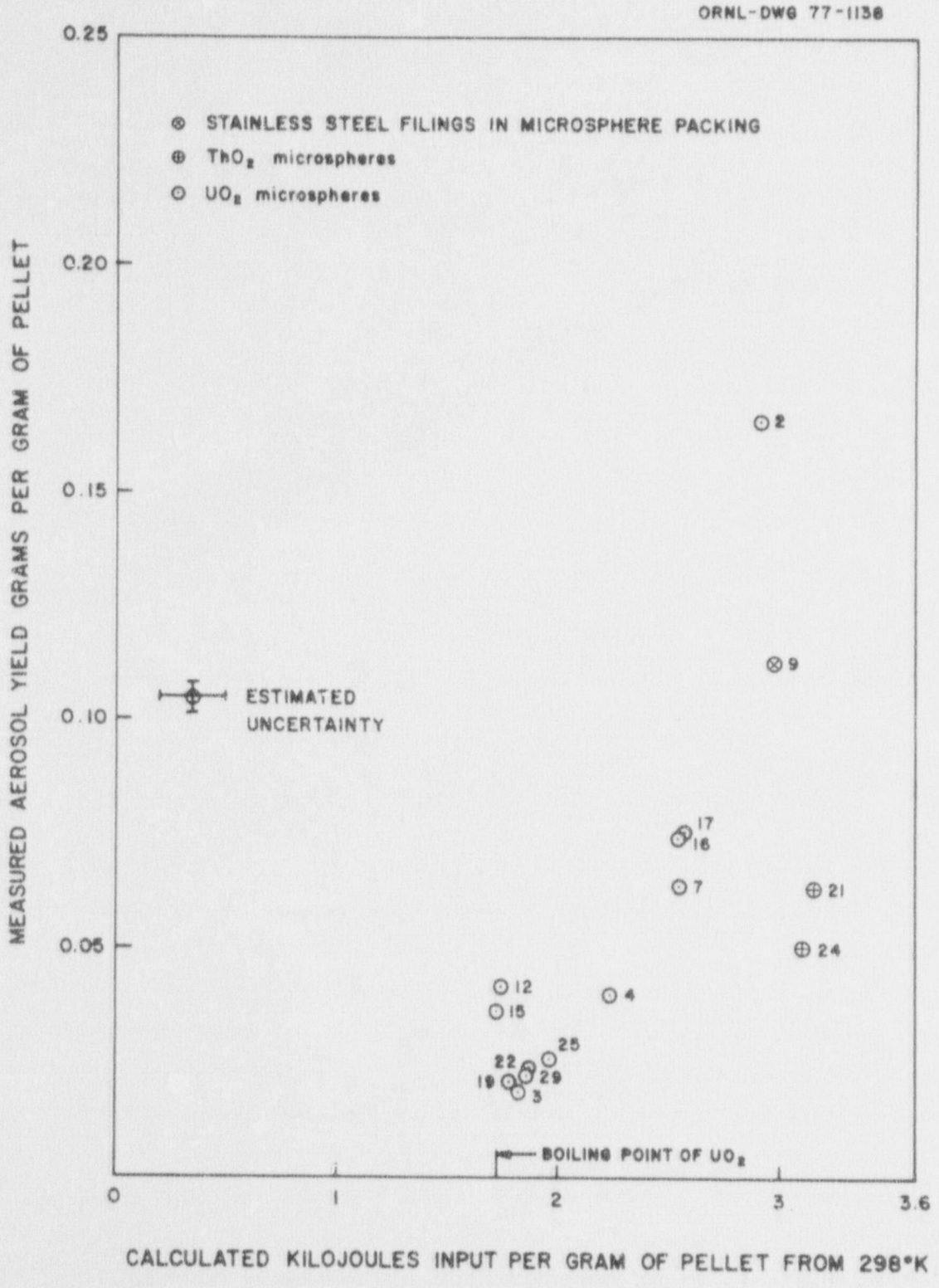

Fig. 2.9. Aerosol yield as a function of energy density for CRI-III tests.

Table 2.3. Firing conditions and results for energy density tests

CDV No.	CDV power[a] (MW/g)	High preheat power[a] (W/g)	CDV energy[a] (J/g)	Net J/g from 298 K[a]	Aerosol yield[a] (g/g)
2	0.64	87	1240	2910	0.166
3	0.34	95	152	1832	0.018
4	1.21	100	548	2228	0.040
7	1.02	100	880	2560	0.064
12	0.38	98	124	1754	0.042
15	0.81	82	131	1731	0.038
16	0.64	71	960	2560	0.075
17	0.62	75	1080	2690	0.076
19	0.40	83	150	1790	0.021
22	0.60	72	263	1873	0.023
25	0.59	75	364	1974	0.026
29	0.49	86	188	1848	0.023
9	0.99	100	1292	2967	0.113
21	0.45	100	1540	3160	0.064
24	0.40	100	1500	3110	0.050

[a]Per gram of pellet; based on pellet mass given in Table 2.1.

The particle size distributions produced in CRI-III tests will be discussed in Section 4. Electron photomicrograph grids were used to collect particles from plateout or electrostatic precipitator samples. Photographs of these grids taken at 5000 to 30,000× were used to determine the size distribution by measuring the sizes and counting the number of particles in a given size range. The method of collection and length of sampling time apparently did not influence the size distribution.

3. PREDICTION OF AEROSOL YIELD AS A FUNCTION OF ENERGY DENSITY

3.1 Introduction

The purpose of the analysis described in this section is to predict the dependence of initial aerosol (vapor) yield in the CRI-III tests on energy density in the UO_2 pellets after capacitor discharge. Calculations described below, except for low CDV energy inputs, predict yields much higher than those that have been experimentally determined. Possible reasons for these differences are discussed below.

3.2 Analysis to Predict CRI-III Test Aerosol Yield

The theoretical modeling to predict the aerosol yield in CRI-III experiments can be divided into three phases: preheat, capacitor discharge, and expansion after quartz rupture.

The pellet stack was assumed to be fully molten after preheat (this assumption was verified experimentally). The preheat steady-state temperature distribution through the pellet stack was estimated by modeling the configuration of UO_2 pellets and microspheres as concentric cylindrical regions and equating the sum of the electrical energy deposited into each region (for a given region temperature, i.e., resistivity) with the radiation heat loss from the outer microsphere surface. An iterative procedure is used to match measured and calculated preheat power. Thermal expansion is accounted for by holding known region masses fixed while adjusting radial boundaries according to saturation densities at the calculated region temperatures. Boundaries are held fixed for partially voided regions, and excess liquid UO_2 is moved into adjacent available void space where mass mean temperatures are calculated. The "pellet mass" is then redefined as the mass contained in all regions with no void space. A sample calculated temperature distribution for test 17 (preheat power = 2200 W) is shown in Fig. 3.1.

Two similar models were used for the energy input during capacitor discharge. In the model developed by Kelly,[2] the energy addition by capacitor discharge was assumed to be so rapid that heat losses and

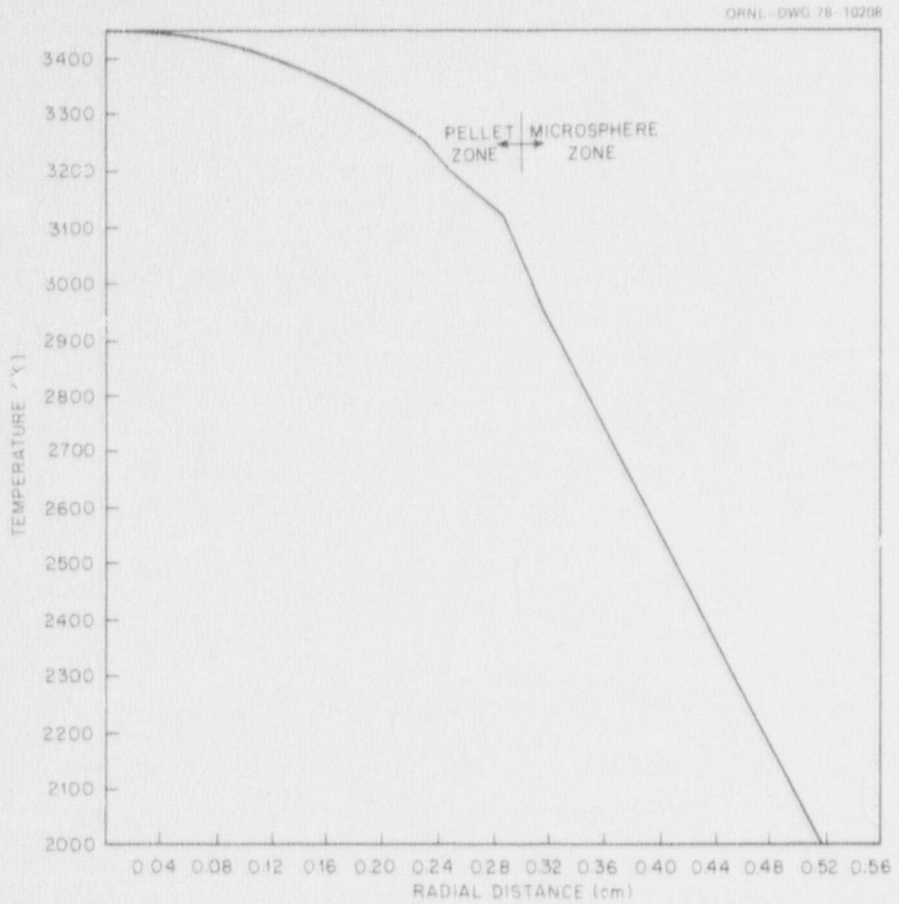

Fig. 3.1. Calculated pellet/microsphere temperature distribution after preheat for test 17.

internal heat transfer are negligible. The power distribution in the sample is assumed to be spatially dependent on the local temperature. The test sample is divided into concentric cylindrical regions with the region boundaries held fixed. Because heat losses and heat exchange between nodes are neglected, an arbitrary rate of power addition can be used. Electrical energy is added to the pellet regions at a rate of 15 MW per 10-μsec time step.

At the start of each time step, temperature dependent equations are used to calculate the region densities and their electrical conductivities. For the arbitrarily fixed power addition rate, a pseudovoltage can be calculated from the total sample resistance (parallel conductors). The distribution of the energy deposition into each region is then determined

from the voltage and each separate region conductance. The local energy addition over the time step is allocated to the heat of fusion and to sensible heat. Because node boundaries are fixed and liquid densities are assumed to be at the saturation values, the calculated mass in a given node will vary with time. Excess liquid UO_2 calculated in a given time step is moved arbitrarily to outer adjacent regions, and mean temperatures are calculated for those regions. Calculations are continued in time until a given total energy input is reached.

The second modeling tool used for the capacitor discharge phase was a modified version of the PAD code,[3] a one-dimensional reactor disassembly code. The modifications to the PAD code essentially consisted of removing all consideration for neutronic prompt-critical power generation and replacing this with electric power generation equations similar to those used in Kelly's model.

The power routine inputs a time history of measured voltage and current through the test sample. Finite-region electrical resistances, again functions of temperature, are used to determine region currents normalized to match the total input current. The calculated energy deposited into each region is then determined from the voltage and region current.

The thermodynamic routine allows energy to be allocated to the following areas: heat of fusion, heat of vaporization, expansion work, and sensible heat. An energy balance is used to determine the temperature distribution throughout the test sample; region pressures are then determined from a density- and temperature-dependent equation of state. The vapor fraction is determined by equating pressures from the perfect gas equation of state and an integral form of the Clausius-Clapeyron equation.

The driving force for material motion, which occurs in the radial direction in the 1-D PAD code, is the pressure difference between adjacent regions. Boundaries of partially voided regions are held fixed throughout the calculation; thus, region temperatures can increase only due to direct electrical energy deposition.

Each approach (Kelly's code and PAD) produces an energy and temperature distribution in the fuel pellets and in the microspheres at the end

of the capacitor discharge phase. A sample calculated temperature distribution using the PAD code (for test 17) is shown in Fig. 3.2. An estimate of the vapor yield is then made by assuming that the material in each concentric region in the pellet stack flashes and vaporizes independently of material in other regions.

The vaporization process was treated as an equilibrium thermodynamic process. An overestimate of the expected yield can be obtained by assuming that the expansion is adiabatic with no work being done on the surroundings (constant internal energy). A less conservative estimate of the yield is made by assuming an isentropic expansion. The appendix contains a description of these calculations.

A plot of percent vapor yield as a function of energy density in a pellet region is shown in Fig. 3.3. The curves for both constant internal energy and isentropic expansion yields are essentially linear with respect

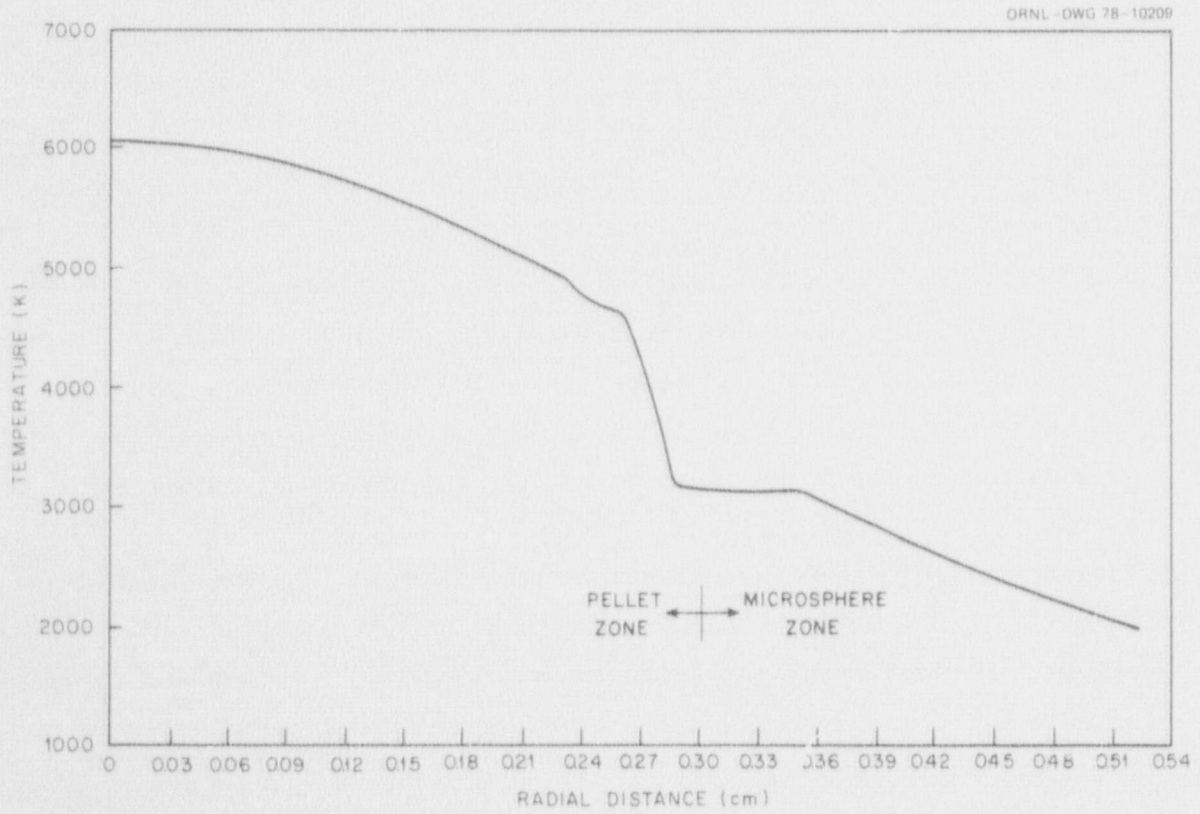

Fig. 3.2. Calculated pellet/microsphere temperature distribution after capacitor discharge for test 17 (using PAD code).

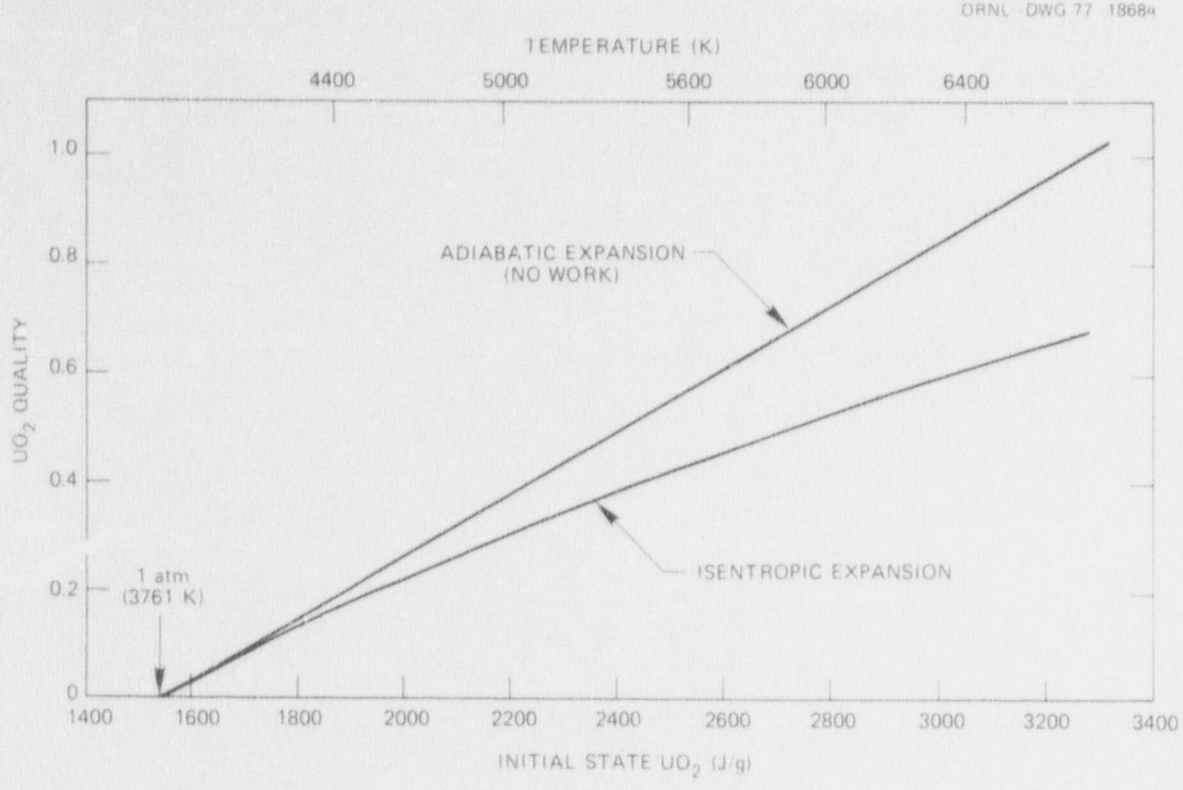

Fig. 3.3. UO_2 quality after expansion as a function of initial saturated liquid state.

to energy level. This implies that the UO_2 vapor quality can be estimated based on the average temperature (energy) in the UO_2, provided that all regions are above the UO_2 boiling point.

3.3 Interpretation of Results

Table 3.1 presents the calculated results for tests 7, 17, and 19, using Kelly's code and the PAD code for both constant internal energy and isentropic assumptions. A comparison of the calculated results for isentropic expansion with representative experimental data is shown in Fig. 3.4.

The computer model greatly overpredicts the yield for higher energy densities (e.g., tests 7 and 17) but predicts a somewhat lower yield for the test with low energy density (test 19). Predictions for tests 7 and 17 are about a factor of 5 greater than measured values. The predicted

Table 3.1. Experimental and calculated yield results for CRI-III tests 7, 17, and 19

Test	Experimental yield (g)	Theoretical yield (g)			
		Isentropic		Constant internal energy	
		PAD	Kelly	PAD	Kelly
7	1.14	5.83	4.83	7.14	6.13
17	1.67	8.23	5.27	10.58	6.79
19	0.45	0.012	0.143	0.014	0.160

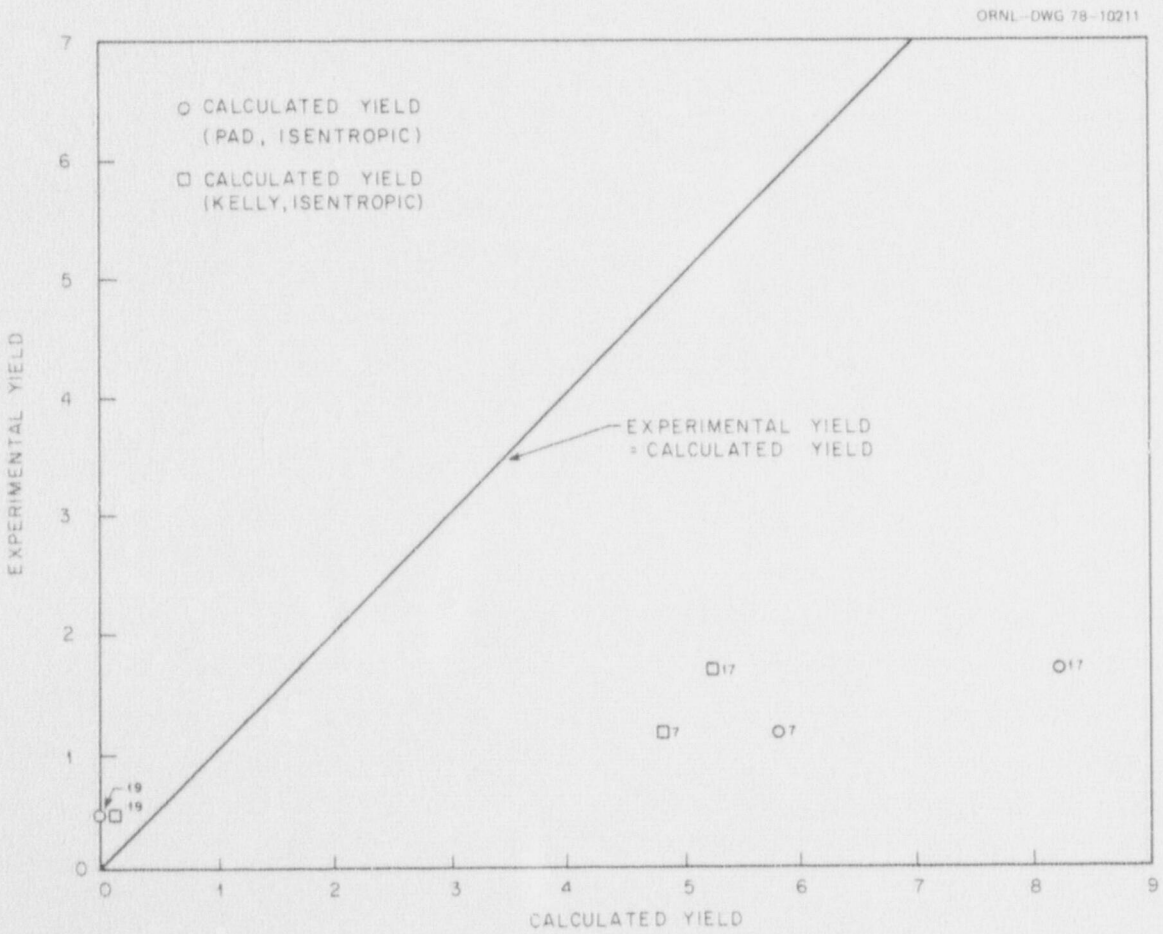

Fig. 3.4. Calculated and experimental aerosol yield vs energy input.

yield is less than that measured for test 19; however, if a somewhat greater energy deposition that was still within the experimental uncertainty was assumed for test 19, the predicted yield could be equal to that measured.

Yields predicted using the PAD and Kelly codes are smaller than those predicted by assuming a uniform energy state because of differences in model equations of state and some redistribution of energy. For example, Kelly's code includes energy redistribution due to the pseudo-transport of hot liquid UO_2 into the colder microsphere region.

Speculated effects that might account for the differences in calculated and measured yields include (1) energy losses during the capacitor discharge phase, (2) energy losses during the flashing of liquid to vapor, and (3) errors in measuring the initial aerosol yield.

Energy loss mechanisms that were investigated and found to be negligible were (1) the kinetic energy imparted to the liquid fragments during expansion, (2) radiation heat loss between the time of preheat cutoff and capacitor discharge, and (3) the energy necessary to produce small droplets by fragmentation.

A mechanism for energy redistribution during capacitor discharge is the potential movement of hot liquid UO_2 into the cooler microsphere region. This mass removal from the region of greatest energy input reduces the quantity of liquid that can potentially produce vapor. Kelly's code simulates this effect by arbitrarily moving excess pellet liquid (change in volume due to thermal expansion) into the microsphere region. This technique accounts for part of the yield discrepancy (see Fig. 3.4); therefore, improvements in the modeling of this mechanism will be continued to obtain a better estimate of its effect on vapor yield.

A sensitivity study using the PAD code is also being conducted. Such a study should delineate the range of calculated yields that could result from lack of precise knowledge of UO_2 properties such as specific heat, electrical and thermal conductivity, and the vapor-pressure relationship.

Any energy lost from the liquid UO_2 before production of vapor will reduce the yield. Figure 3.5 illustrates the calculated reduction of

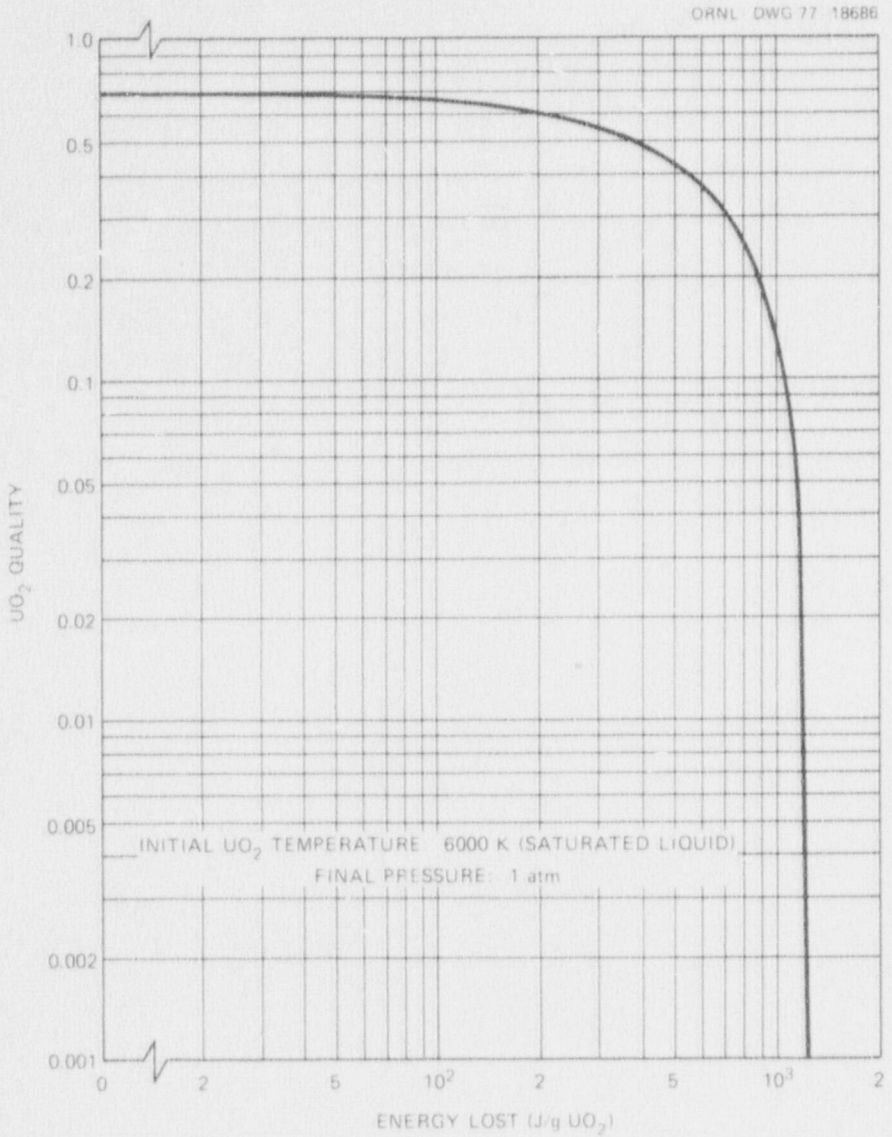

Fig. 3.5. UO_2 quality vs energy lost during expansion.

adiabatic expansion fuel quality for arbitrary energy losses. The initial UO_2 condition for this figure is assumed to be saturated liquid at 6000 K (which was approximately the energy content of the UO_2 pellets in tests 7 and 17), and the final pressure after expansion is taken to be 0.101 MPa (1 atm). Two heat loss mechanisms that could occur during expansion are (1) liquid UO_2 may lose heat by radiation rapidly at the expense of vapor production; (2) vapor may recondense onto UO_2 microspheres, which have a large surface area and could be ∿1000 K cooler than the vapor.

After quartz breakup, UO_2 is assumed to be in the form of droplets at temperatures greater than 4000 K. Radiation cooling may rapidly reduce the liquid temperature to that corresponding to 1 atm pressure (the surrounding argon pressure), below which vapor will not be produced. Drop cooling times can be estimated by a lumped system analysis for the liquid temperature T_ℓ. The governing equation is

$$\rho C_p V \frac{dT_\ell}{dt} = -A\varepsilon\sigma T_\ell^4 \ , \tag{3.1}$$

where

$V = \frac{4}{3}\pi r^3$,

$A = 4\pi r^2$,

r = drop radius,

ρ = liquid density, assuming ρ (5000 K) = 8.1 g/cm^3 (Ref. 4) is representative,

C_p = 0.62 J/g-K,

σ = 5.67 (10^{-12}) W/cm^2-K (assume $\varepsilon \simeq 1$).

Equation (3.1) can be solved to give the time t_c required for a drop to cool from T_i to T_f = 3761 K, saturation temperature at 1 atm, as follows:

$$t_c = \frac{\rho C_p r}{9\sigma}\left(T_f^{-3} - T_i^{-3}\right) \ . \tag{3.2}$$

Table 3.2 presents estimated cooling times for values of T_i and drop radius r. Note that these times are of the order of 1 msec or less for drops of 10 μm (0.001 cm) radius. This indicates that radiation cooling can be a powerful heat loss mechanism if the drop sizes produced are small.

If the rate of radiation heat cooling is comparable to or greater than the net evaporation rate, much of the potential for vapor formation could be lost.

A kinetic theory expression for the evaporation rate (neglecting self-condensation) is[5]

$$\text{Evaporation rate} = \frac{\sigma_e P_{sat}(T_\ell)}{\sqrt{2\pi R T_\ell}} \ \text{g/cm}^2\text{-sec} \ , \tag{3.3}$$

Table 3.2. Drop cooling times for different initial temperatures and drop sizes

T_i (K)	r (μm)	t_c (sec)
6000	1000	0.139
	100	1.4×10^{-2}
	10	1.4×10^{-3}
5000	1000	0.106
	100	1.1×10^{-2}
	10	1.1×10^{-3}
4000	1000	3.1×10^{-2}
	100	3.1×10^{-3}
	10	3.1×10^{-4}

where σ_e = an accommodation coefficient and $P_{sat}(T_\ell)$ = UO_2 saturation pressure at T_ℓ^4 = exp $[-4.34\ \ell n(T_\ell) - (76800/T_\ell) + 69.979]$ dynes/cm^2. The comparable equivalent amount of heat loss due to evaporation is

$$\text{Evaporation heat loss} = EL = \frac{\sigma_e P_{sat}(T_\ell) h_{\ell v}}{\sqrt{2\pi R T_\ell}} \text{ J/cm}^2\text{-sec}, \qquad (3.4)$$

where $h_{\ell v} \simeq 1800$ J/g for UO_2.

Table 3.3 shows EL compared with the radiation heat loss rate, assuming $\sigma_e = 1$ and $\varepsilon = 1$. For $\sigma_e = 1$, evaporation rates are much greater than radiation heat loss rates. However, $\sigma_e = 1$ is the theoretical upper limit, and, in fact, $\sigma_e \ll 1$ is not unrealistic. If σ_e is of the order of 0.01, radiation heat loss will certainly become important. In addition, we have not accounted for recondensation of vapor on drops, which would reduce the net evaporation heat loss rate.

Radiation heat loss could also be important in a reactor accident because fuel will be at very high temperatures. In addition, the bubble expansion time is tens of milliseconds in a reactor, meaning that radiant loss could be even more important than in the CDV tests, where expansion times are much shorter.

Table 3.3. Comparison of evaporation and radiation heat loss rates for $\sigma_e = 1$, $\varepsilon = 1$

$$EL = \frac{\sigma_e P_{sat}(T_\ell) h_{\ell v}}{\sqrt{2\pi R T_\ell}} \quad , \quad RL = \varepsilon \sigma T_\ell^4$$

T_ℓ (K)	EL (J/cm^2-sec)	RL (J/cm^2-sec)	EL/RL
6000	4.55×10^6	7.35×10^3	619
5000	8.51×10^5	3.54×10^3	240
4000	5.38×10^4	1.45×10^3	37

Condensation on the cold microspheres could also reduce the apparent vapor yield because of their low temperature [$\sim$2500 K (4041°F) after CDV discharge] and large surface area. A simple scoping analysis was used to estimate the magnitude of this effect. A solution of the heat equation in spherical coordinates, assuming constant initial microsphere temperature and constant surface temperature for $t > 0$ gives:[6]

$$T_s = T_0 + (T_{s_0} - T_0)\left[1 + \frac{2a}{r}\sum_{n=1}^{\infty}\frac{(-1)^n}{n}\sin\left(\frac{n\pi r}{a}\right)e^{-\alpha_s n^2\pi^2 t/a^2}\right] , \qquad (3.5)$$

where

a = microsphere radius,

r = radial coordinate,

T_s = microsphere temperature = $T_s(r,t)$,

T_0 = initial microsphere temperature, assumed to be 2500 K (4041°F),

T_{s_0} = drop surface temperature,

α_s = UO_2 thermal diffusivity $\approx 4.84(10^{-3})\ \frac{cm^2}{s}$.

The heat gained by a microsphere per unit surface area, assumed to be due to condensation, is

$$q_c = \int_0^t k_s \left.\frac{dT}{dr}\right|_a dt = \frac{2k_s(T_{s_0} - T_0)a}{\alpha_s \pi^2}\sum_{n=1}^{\infty}\frac{1}{n^2}\left(1 - e^{-\alpha_s n^2\pi^2 t/a^2}\right) , \qquad (3.6)$$

where k_s = UO_2 thermal conductivity $\approx$ 0.03 W/cm-K.

Microspheres used in CRI-III tests were from 0.018 cm (0.007 in.) to 0.025 cm (0.010 in.) in radius. Assuming a total microsphere mass of 36 g and a microsphere surface temperature of T_{s_0} = 3761 K (6310°F) (saturation temperature at 1 atm pressure), values of possible heat loss due to condensation on microspheres were calculated. These are presented in Table 3.4.

Table 3.4. Estimated heat loss to microspheres for various sphere sizes and contact times

Contact time (msec)	a (cm)	Q_c (J)
0.1	0.025	2389
	0.018	3291
1	0.025	7141
	0.018	9609

For a UO_2 heat of vaporization of 1800 J/g, these calculations indicate that more than 5 g of vapor could condense in a contact time of 1 msec. However, contact times are likely to be of the order of 0.1 msec or less — the time scale for vapor to convert to an aerosol. For a 0.1-msec contact time, approximately 2 g of vapor could condense. This would account for part (roughly a factor of 2) of the factor of 5 difference in experimental and calculated vapor yields at high UO_2 energy densities.

Future tests must be relied on to determine the amount of condensation on microspheres. Possible ways to evaluate condensation on microspheres in future tests are to (1) change the microsphere size (and thus the microsphere surface available for condensation) to determine the effect on the aerosol yield; and (2) use thorium oxide microspheres which could be collected and chemically analyzed after a test to determine how much UO_2 had condensed onto them.

Certain aspects of the experimental procedure suggest that the determination of the measured yield may be lower than that which is actually

produced in the CRI-III tests. The major possibility for error is in the estimate of the initial aerosol concentration from the plot of aerosol concentration vs time. As discussed in the explanation of data reduction in Section 2, aerosol mass measurements commence ∿2 min after a test begins. The initial (time = 0) aerosol concentration is estimated by fitting a first-order exponential ~ -ve to the first few data points in the plot of concentration vs time. Some concentration vs time data are presented in Fig. 2.8.

The trend of the data in Fig. 2.8 for tests 21 and 24 indicates that very rapid changes in the aerosol concentration are occurring early in the transient, meaning that initial concentrations could exceed present estimates. In future tests, mass sampling will be performed automatically as soon as possible to provide a better estimate of the yield. This will be accomplished by installing solenoid valves in the mass sampling system.

Other possible aerosol loss mechanisms are plateout of liquid and condensation of vapor on the vaporizer housing and aerosol plateout on the side walls of the lower portion of the CRI-III vessel (see Fig. 2.1). After the first 15 CRI-III tests, the vaporizer design was changed to minimize cool structure previously in the path of expanding material; this change appears to have had little effect on aerosol yield. However in future tests the housing will be examined in an attempt to determine the actual amount of material deposited there.

After capacitor discharge, the aerosol expands from a confined area into the entire vessel volume. To determine whether much of the aerosol has plated on the lower vessel walls, tests should be performed with the vaporizer mounted at the vessel midline so that adjacent wall structure is less likely to interfere with the expanding aerosol cloud.

4. SIZE DISTRIBUTION OF PRIMARY PARTICLES PRODUCED IN CRI-III/CDV TESTS

An important measurement in the CRI-III/CDV tests is the determination of the size distribution of the "primary" aerosol particles. The dependence of the size distribution on energy density and the nature of the distribution are discussed here, as is the possible importance of these results in assessing the consequences of HCDAs.

CDV-produced aerosol agglomerates are collected on both diffusion and electrostatic grid precipitators for observation under a transmission electron microscope. Figure 4.1 is a photomicrograph of a typical CDV UO_2 aerosol. These high-magnification photographs are analyzed by manually counting and measuring the particle sizes.

Three CDV tests at low energy density (tests 19, 22, and 29) and three at high energy density (tests 16, 21, and 24) were selected for detailed primary particle size analysis. Figure 4.2 is a histogram of the number of particles in logarithmically selected size groups for four of the tests. (Tests 19 and 22 were omitted for clarity; however, they showed the same, almost identical, size distributions as the other runs.) The figure shows that under the conditions of aerosol formation in CRI-III, the variation in energy density for these tests (approximately 1400 J/g) does not significantly affect the size and distribution of the primary particles.

Figure 4.2 also shows a similar histogram from an earlier CDV test (AEDC-14) in a different vessel. The energy density for AEDC-14 was comparable to that for the three high-energy density tests shown in the figure. The only significant difference between this test and CRI-III tests is the total volume of the vessel into which the aerosol was released; the slightly different primary size measured for AEDC-14 does not appear significant.

The composite cumulative number distribution for the six tests is shown on log-normal coordinates in Fig. 4.3 along with the same data converted to a mass basis assuming spherical particles of density of 10.9 g/cm^3. The primary particles have a log-normal distribution with a mean geometric diameter of $d_g = 0.014$ μ and a standard deviation of

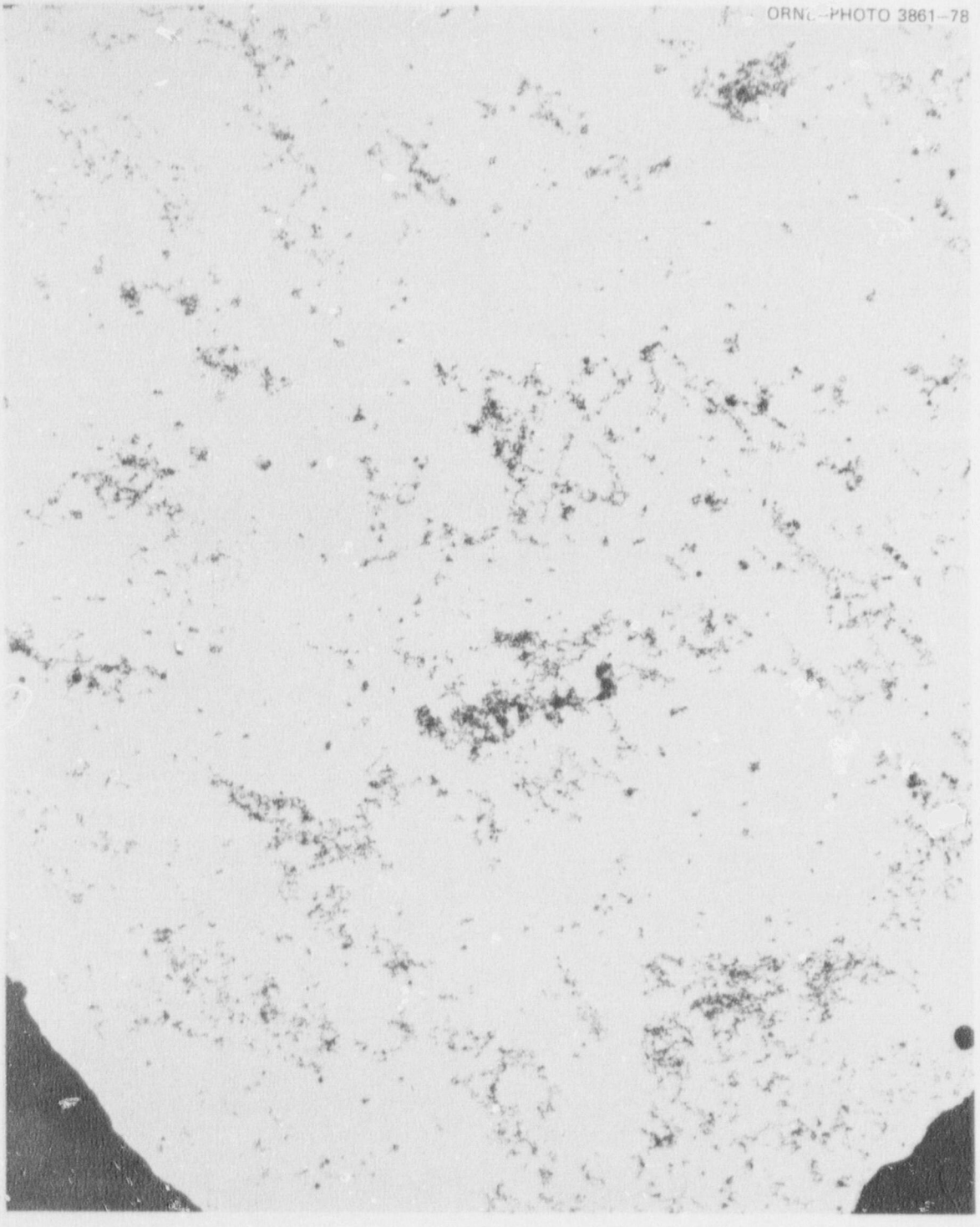

Fig. 4.1. Photomicrograph of agglomerated CDV aerosol from test 21 (5000×).

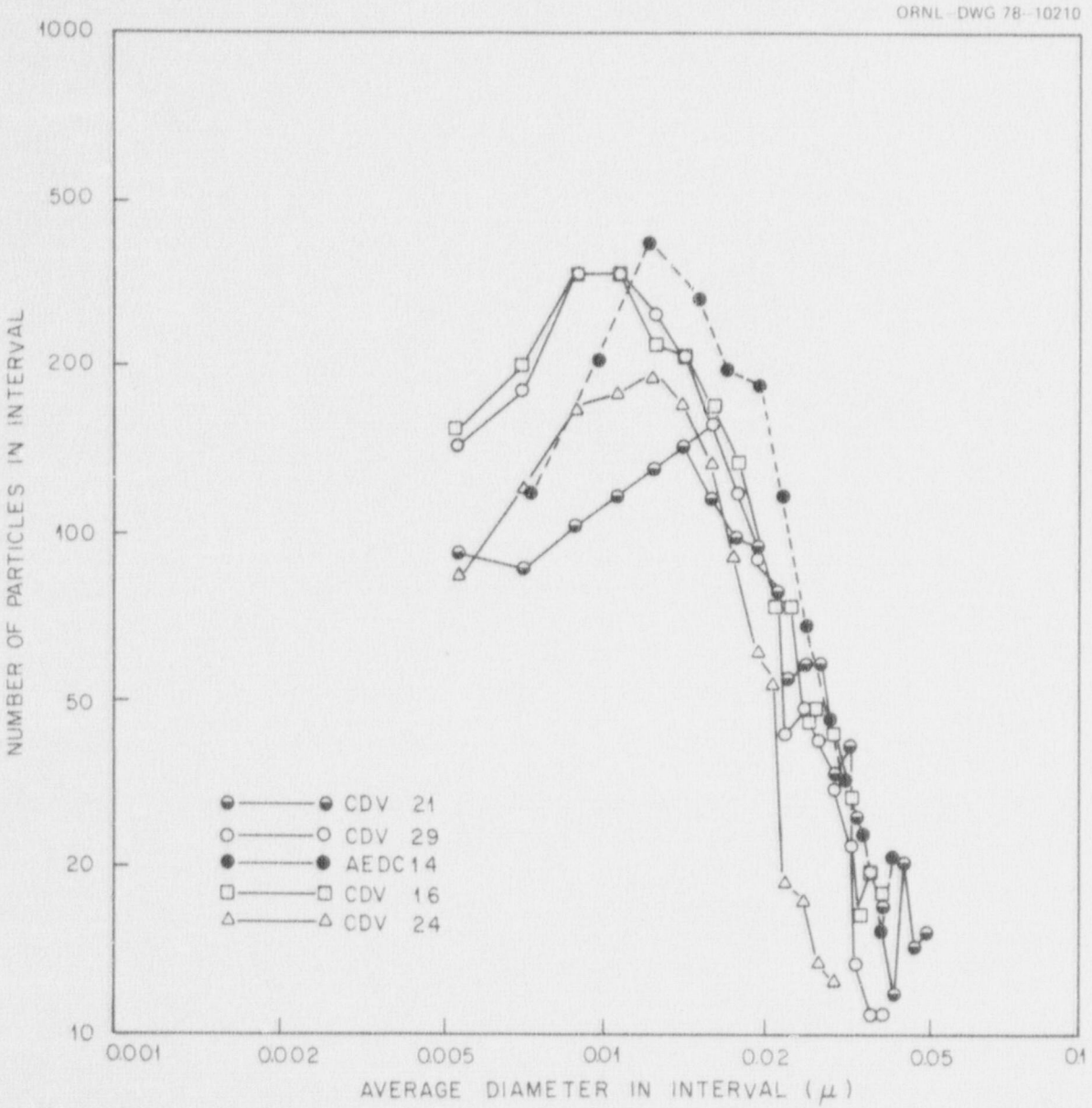

Fig. 4.2. Electron photomicrograph numerical counts vs particle size for individual tests.

σ_g = 1.8. Although >99% of the particles have diameters less than 0.06 μ, about 60% of the total mass resides in these particles.

Figure 4.4 presents cascade impactor measurements of agglomerate "aerodynamic" diameters at different times during the aerosol transient in three CRI-III tests. These diameters also follow a log-normal distribution and have a mean diameter (d_{50}) that apparently increases later in the transient.

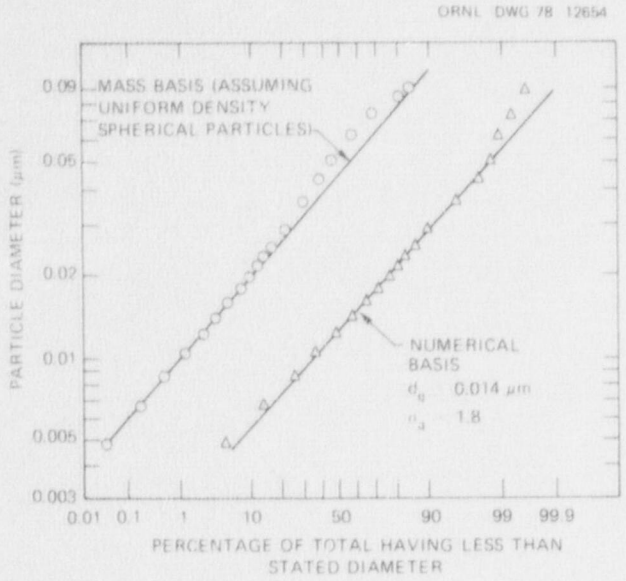

Fig. 4.3. Primary particle size distribution for CRI-III experiments from electron photomicrograph counts (5330 total particles).

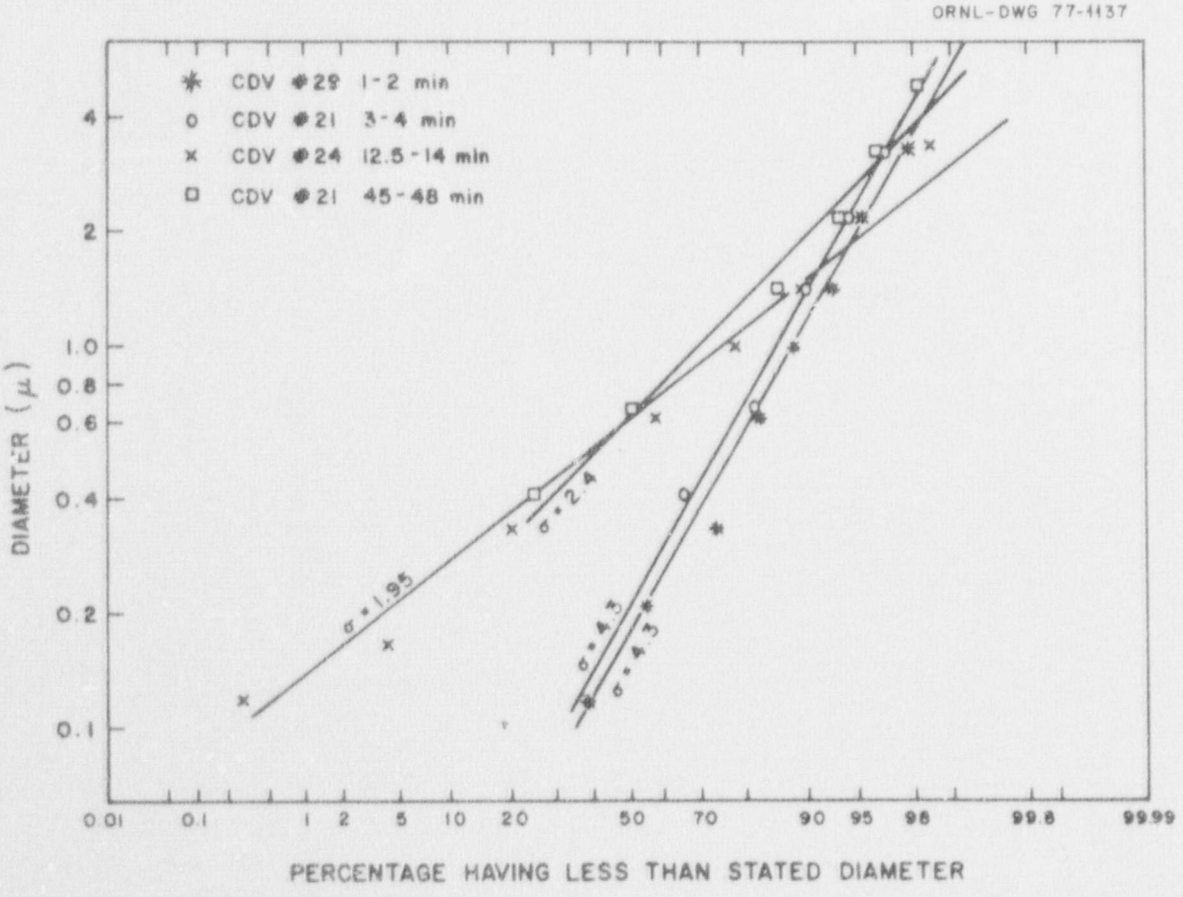

Fig. 4.4. CRI-III aerosol aerodynamic diameter data from cascade impactor measurements.

The importance of the primary size distribution measurements in assessing the consequences of an HCDA is somewhat uncertain at this time. Due to rapid agglomeration of aerosols at high concentrations in an HCDA bubble, the "source" aerosol size (as it may be released into the secondary containment) may bear little relationship to the size of the primary aerosols initially formed by nucleation and growth from the vapor state.

For example, a simple scoping calculation for an HCDA can be made by assuming that the HCDA bubble volume is $\sim$24.9 m^3 (880 ft^3, the cover gas volume), of which about 20% is made up of noncondensable fission gases and the rest of fuel vapor ($\sim 5 \times 10^5$ g).[7] Assuming that all the vapor becomes an aerosol of 0.001 μm in diameter and occupies the same volume as the noncondensables, the number density would be

$$(n)_{0.001\ \mu m} \simeq 10^{19}\ \text{particles/cm}^3 .$$

If the aerosol size were much larger, 1 μm in diameter, the number density would be

$$(n)_{1\ \mu m} \simeq 10^{19} \left(\frac{0.001}{1}\right)^3 = 10^{10}\ \text{particles/cm}^3 .$$

It can easily be shown from the Smoluchowski equation[8] for coagulation of monodisperse fuel aerosols [$(dn/dt) = -Kn^2$, n = number density] that as long as n is greater than about 10^{11} particles/cm^3, only a fraction of a second is required for rapid agglomeration to reduce the number density to 10^{10} particles/cm^3. Moreover, the time required to reach this number density is not significantly increased for an arbitrarily higher number density. Since the HCDA bubble rise time has been estimated to be $\sim$1 to 2 sec, there is ample time for the aerosol to increase in size before the bubble has risen significantly.

The significance of the primary size distribution may therefore lie in the potential influence of the initial size on the characteristics and behavior of the resulting agglomerates. A 1-μm-diam (equivalent) aerosol particle made up of chains of many 0.001-μm primaries may behave aerodynamically differently than a similar-sized particle made up, for instance, of chains of 0.01-μm primary particles.

In addition, it is possible that the release into the secondary containment may consist partially of fuel vapor that has not yet condensed into an aerosol. In this event, vapor quenching in the secondary containment would produce primary-sized particles at low enough number densities that significant time would be required to produce larger sizes.

The potential effect of small aerosol sizes on the quantity of aerosol that may leak into the atmosphere from the secondary containment can be calculated using the HAARM-2 code.[9] Figure 4.5 shows the result of a calculation for two greatly different assumed initial aerosol mean sizes with a given initial concentration of 10 g/m^3 and a given leak rate of 0.1 vol %/day. The figure indicates that for direct release of fuel vapor into the secondary containment, a difference in initial size of

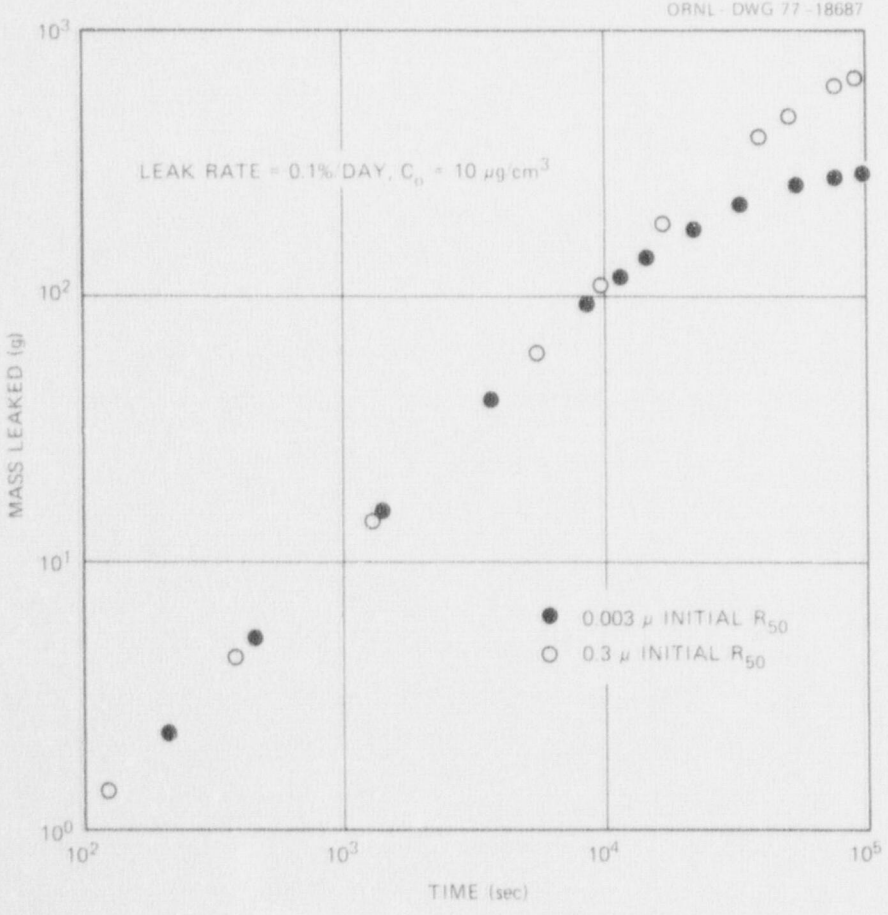

Fig. 4.5. Aerosol mass leakage from a secondary containment-sized vessel (using the HAARM-2 code[9]) for different R_{50} values.

the primary aerosol "source" could be significant in determining the total that could potentially leak to the atmosphere.

In the Fuel Aerosol Simulant Tests,[10] the CDV technique will be used to produce UO_2 vapor bubbles under water and under sodium. Aerosol may be produced during bubble expansion — which will occur in ~10 msec rather than the 1 msec in CRI-III tests — and during bubble rise, which may take as long as 2 sec. Thus the CRI-III particle size measurements will also provide an important basis for comparison with measured size distributions from the FAST experiments.

5. CONCLUSIONS AND RECOMMENDATIONS

The results of tests in the CRI-III/CDV facility to determine the effect of energy density in the UO_2 pellets after capacitor discharge on the resultant initial aerosol (vapor) yield and primary aerosol size distribution were presented and discussed in the previous sections. The major conclusions that were reached are:

1. At high energy content ($\sim$3000 J/g), measured airborne mass yields have been about a factor of 5 less than those that would have been expected from equilibrium thermodynamic expansion calculations. Attempts were made to explain the differences at high energies in terms of potential energy losses and errors in the experimental measurements. Some potential effects were identified, but a definitive explanation for the differences was not established.

2. The primary aerosol sizes were small, ranging from greater than 0.004 to 0.1 μm in diameter. The size distribution was essentially independent of the initial molten UO_2 energy density over the range covered. The size distribution was log-normal, having a mean geometric diameter of 0.014 μ and a standard deviation of 1.8. The measured size data may be useful in synthesizing properties of agglomerates for direct input into aerosol behavioral codes when applied to the HCDA bubble or for cases of direct release of fuel vapor into the secondary containment.

Additional experiments are necessary to determine the differences in yield obtained by measurements and by calculations. Such experiments would fall into two classes: (1) additional tests to determine if the aerosol yield is being measured correctly (described at the end of Section 3), and (2) experiments to isolate different heat loss phenomena that could result in loss of yield. Such tests might entail using larger diameter microspheres in pellet stacks (so that potential vapor condensation on them could be reduced because of their reduced surface area) and performing vaporizations with a material of much lower boiling point, so that the potential for radiation heat loss during expansion would be reduced.

REFERENCES

1. T. S. Kress, G. W. Parker, and M. H. Fontana, *Work Plan: Transient Release from LMFBR Fuel*, ORNL/TM-4875 (September 1975).

2. M. J. Kelly et al., *Development of a Capacitor Discharge Vaporization (CDV) Technique to Produce Aerosols Formed under HCDA Postulated Conditions*, ORNL/NUREG/TM-160 (July 1978).

3. D. M. Peterson, W. R. Stratton, and T. D. McLaughlin, *PAD: A One-Dimensional, Coupled Neutronic Thermodynamic-Hydrodynamic Computer Code*, LA-6540MS (December 1976).

4. M. Kirbiyik, "Fuel-Vapor Generation in LMFBR Core-Disruptive Accidents," Ph.D. dissertation, Nuclear Engineering Department, University of Virginia, 1975.

5. J. G. Refling et al., "Nonequilibrium Evaporation and Condensation in LMFBR Fuel Expansion," in *Bubble Behavior In LMFBR Core Disruptive Accidents*, University of Virginia Report, NUREG-0114, p. 6 (September 1976).

6. H. S. Carslaw and J. C. Jaeger, *Conduction of Heat in Solids*, 2nd ed., p. 233, Oxford University Press, London, 1959.

7. *Preliminary Safety Analysis Report (PSAR)*, Clinch River Breeder Reactor Project, Vol. 10, Appendix D (April 1975).

8. N. A. Fuchs, *The Mechanics of Aerosols*, pp. 288–90, The Macmillan Company, New York, and Pergamon Press, Inc., New York, 1964.

9. L. D. Reed and J. A. Gieseke, *HAARM-2 Users Manual*, BMI-X-665 (1975).

10. A. L. Wright, A. M. Smith, and T. S. Kress, *Fuel Aerosol Simulant Test (FAST) Plan*, ORNL/NUREG/TM-129 (September 1977).

Appendix

METHODS USED TO CALCULATE UO_2 VAPOR QUALITY AFTER EXPANSION

If UO_2 is initially in the saturated liquid state at some elevated temperature T_i, it can flash to a final pressure P_f with a corresponding final temperature T_f and create vapor at some quality χ in the process. The quality will be greatest for an adiabatic expansion, where the system does no work on the surroundings. The internal energy remains a constant for the adiabatic, no-work case as can easily be seen from the first law

$$du = dq - pdv \ , \tag{A.1}$$

where u, q, and v are specific internal energy, heat added to the system, and specific volume, respectively.

A constant internal energy implies

$$U_\ell(T_i) = U_\ell(T_f) + \chi \, U_{\ell g}(T_f) \tag{A.2}$$

for the process; the subscripts ℓ and ℓg refer to the saturated liquid state and to the transition region from saturated liquid to saturated vapor. The quality χ is determined from Eq. (A.2).

The temperature dependence of the specific internal energy of the saturated liquid UO_2 is given by[4]

$$U_\ell(T) = (-122.109 + 0.473014T - 2.36112 \times 10^{-5}T^2 + 4.25418 \times 10^{-9}T^3) \left\{1 + 0.370629 \exp\left[(T - 8010)/130\right]\right\} \ , \tag{A.3}$$

where U is in J/g and T in K. Since the initial temperature is given, the first term on the left can be calculated; the final temperature is the saturation value at the final pressure. The saturation pressure as a function of temperature is given by[4]

$$P_\ell(T) = \exp\left[-4.34 \, \ell n(T) - (76800/T) + 69.979\right] \ , \tag{A.4}$$

where the pressure is in dynes/cm^2 with T in K. Equation (A.4) can be solved for T_f and Eq. (A.3) can be used to solve for $U_\ell(T_f)$.

No correlation was available for $U_{\ell g}(T)$; however, correlations are available for $v_\ell(T)$ and $v_g(T)$. Therefore, use of the Clausius-Clapeyron relation will allow $U_{\ell g}(T)$ to be determined as described below. By the definition of enthalpy,

$$h = U + pv \ . \tag{A.5}$$

Since $U_{\ell g}$ represents a change in the internal energy from the saturated liquid state to the saturated vapor state at constant pressure,

$$h_{\ell g}(T_f) = U_{\ell g}(T_f) + P_\ell(T_f)\ v_{\ell g}(T_f) \ . \tag{A.6}$$

Quantities other than $U_{\ell g}$ must now be determined. The saturated liquid pressure $P_\ell(T_f)$ is given by Eq. (A.4). The change in specific volume from liquid to gas at the final temperature $v_{\ell g}(T_f)$ is obtained by calculating $v_\ell(T_f)$ and $v_g(T_f)$ and subtracting one from the other. These are given by[4]

$$v_\ell(T_f) = \frac{0.33258}{\{1 + 2.51373\ [1 - (T/8000)]^{0.402581}\}}\ \text{cm}^3/\text{g} \ , \tag{A.7}$$

and

$$v_g(T_f) = 4.06768 \times 10^8 [P_\ell(T)]^{-0.924647} \times \{1 - 0.686733 \exp\ [(T - 8000)/200]\}\ \text{cm}^3/\text{g} \ . \tag{A.8}$$

The last term in Eq. (A.6) to be specified is $h_{\ell g}$; this is calculated from the Clausius-Clapeyron equation, that is,

$$\frac{dp(T)}{dT} = \frac{h_{\ell g}(T)}{T v_{\ell g}(T)} \ , \tag{A.9}$$

where the derivative is taken along the liquid saturation curve. The saturated-liquid pressure is given by Eq. (A.4), and its derivative is

$$\frac{dp(T)}{dT} = (76800T^{-6.34} - 4.34T^{-5.34}) \exp\ [(-76800/T) + 69.979] \ . \tag{A.10}$$

Hence, $h_{\ell g}$ can be calculated, thus allowing $U_{\ell g}$ and finally the quality χ to be found.

As mentioned in the text, an adiabatic-isentropic expansion is probably more realistic because the work done on the surrounding medium by the expanding vapor is included. The quality calculated in this manner will be less than that for the adiabatic, no-work, expansion.

For this process, entropy is conserved by definition; therefore,

$$s_{\ell}(T_i) = s_{\ell}(T_f) + \chi\, s_{\ell g}(T_f) \ . \tag{A.11}$$

This equation can be solved for the quality χ. The specific entropy of saturated liquid UO_2 at temperature T(K) is given by[4]

$$\begin{aligned} s_{\ell}(T) = {} & -3.8067196 + 0.473014\ \ell n\ T - 4.72224 \times 10^{-5} T \\ & + 6.38125 \times 10^{-9} T^2 + (0.17415 - 8.546 \times 10^{-6} T \\ & + 1.57672 \times 10^{-9} T^2)\ \exp\ [(T - 8010)/130] \\ & + \exp\ (-67.9445 + 2.36358 \times 10^{-2} T - 3.38261 \times 10^{-6} T^2 \\ & \qquad + 1.74433 \times 10^{-10} T^3)(J/g\text{-}K) \ . \end{aligned} \tag{A.12}$$

In order to calculate $s_{\ell g}(T_f)$, one again makes use of the Clausius-Clapeyron equation (A.9), where $h_{\ell g}(T_f)$ and $v_{\ell g}(T_f)$ are quantities associated with constant temperature and pressure processes along the saturated liquid line. From the standard thermodynamic relation,

$$T\, ds = dh - v\, dp \ , \tag{A.13}$$

and it follows that

$$T\, ds = dh \tag{A.14}$$

at constant pressure. Hence,

$$s_{\ell g}(T) = \frac{h_{\ell g}(T)}{T} \ , \tag{A.15}$$

and substitution into Eq. (A.9) gives

$$\left[\frac{dp(T)}{dT}\right]_{T_f} = \frac{s_{\ell g}(T_f)}{v_{\ell g}(T_f)} , \qquad (A.16)$$

from which $s_{\ell g}$ can be calculated. Therefore, all specific entropies in Eq. (A.11) can be calculated, allowing the quality χ to be determined.

The methods outlined above allow the calculation of the quality, given an initial temperature and final pressure, for the limiting case of an adiabatic expansion, no-work case, and for a more realistic isentropic expansion. The outputs from both the Kelly and the PAD codes give the final temperature of each cylindrical region and also the mass of each region at the end of the capacitor discharge just prior to quartz rupture. The total vapor fraction was then calculated by finding (by the methods described above) the quality to be expected from each cylinder upon independent expansion to the final state, multiplying this quality by the mass of the cylinder, summing such products over all cylinders, and dividing by the initial mass of the fuel pellets.

NUREG/CR-0120
ORNL/NUREG/TM-163
Dist. Category R7

Internal Distribution

1. R. E. Adams
2. M. Bender
3-4. H. W. Bertini
5. J. R. Buchanan
6. W. B. Cottrell
7. G. F. Flanagan
8-9. M. H. Fontana
10. J. T. Han
11. H. W. Hoffman
12. M. J. Kelly
13-14. T. S. Kress
15. Milton Levenson
16. R. E. MacPherson
17. F. R. Mynatt
18. G. W. Parker
19-20. L. F. Parsly
21. P. Patriarca
22. J. M. Rochelle
23. Myrtleen Sheldon
24. A. M. Smith
25. I. Spiewak
26. A. L. Sutton, Jr.
27. D. G. Thomas
28-29. M. L. Tobias
30. H. E. Trammell
31. D. B. Trauger
32. J. L. Wantland
33-35. J. S. White
36. G. D. Whitman
37-41. A. L. Wright
42-43. Central Research Library
44. Y-12 Document Reference Section
45-47. Laboratory Records Department
48. Laboratory Records (RC)

External Distribution

49. J. T. Larkins, Experimental Fast Reactor Safety Research Branch, RSR-NRC
50. Director, Research and Technical Support Division, DOE,ORO
51-360. Given distribution as shown in category R7 (25 copies — NTIS)

120555003927 1 R7
US NRC
SECY PUBLIC DOCUMENT ROOM
BRANCH CHIEF
HST LOBBY
WASHINGTON DC 20555